

# An ancestral interaction module promotes oligomerization in divergent mitochondrial ATP synthases

Alexey Amunts (✉ [amunts@scilifelab.se](mailto:amunts@scilifelab.se))

Stockholm University <https://orcid.org/0000-0002-5302-1740>

Ondrej Gahura

Institute of Parasitology, Biology Centre CAS <https://orcid.org/0000-0002-2925-4763>

Alexander Muhleip

Stockholm University <https://orcid.org/0000-0002-1877-2282>

Carolina Hierro-Yap

Institute of Parasitology, Biology Centre CAS

Brian Panicucci

Biology Centre

Minal Jain

Institute of Parasitology, Biology Centre CAS

David Hollaus

Institute of Parasitology, Biology Centre CAS <https://orcid.org/0000-0001-7403-6434>

Martina Slapničková

Institute of Parasitology, Biology Centre CAS

Alena Zikova

Biology Centre <https://orcid.org/0000-0002-8686-0225>

---

## Article

### Keywords:

**Posted Date:** December 30th, 2021

**DOI:** <https://doi.org/10.21203/rs.3.rs-1196040/v1>

**License:**   This work is licensed under a Creative Commons Attribution 4.0 International License.

[Read Full License](#)

---

**Version of Record:** A version of this preprint was published at Nature Communications on October 11th, 2022. See the published version at <https://doi.org/10.1038/s41467-022-33588-z>.



# 1 An ancestral interaction module promotes oligomerization in divergent 2 mitochondrial ATP synthases

3  
4 Ondřej Gahura<sup>1,†</sup>, Alexander Mühleip<sup>2,†</sup>, Carolina Hierro-Yap<sup>1,3</sup>, Brian Panicucci<sup>1</sup>, Minal  
5 Jain<sup>1,3</sup>, David Hollaus<sup>3</sup>, Martina Slapničková<sup>1</sup>, Alena Zíková<sup>1,3,\*</sup>, Alexey Amunts<sup>2,4\*</sup>

6  
7 <sup>1</sup>Institute of Parasitology, Biology Centre CAS, Ceske Budejovice, Czech Republic

8 <sup>2</sup>Science for Life Laboratory, Department of Biochemistry and Biophysics, Stockholm  
9 University, 17165 Solna, Sweden

10 <sup>3</sup>Faculty of Science, University of South Bohemia, Ceske Budejovice, Czech Republic

11 <sup>4</sup>Department of Physiology and Pharmacology, Karolinska Institutet, Stockholm, Sweden

12  
13  
14  
15 \* Correspondence to: [azikova@paru.cas.cz](mailto:azikova@paru.cas.cz); [amunts@scilifelab.se](mailto:amunts@scilifelab.se)

16 † These authors contributed equally to this work.

## 17 18 19 **Abstract**

20 Mitochondrial ATP synthase forms stable dimers arranged into oligomeric assemblies that  
21 generate the inner-membrane curvature essential for efficient energy conversion. Here, we  
22 report cryo-EM structures of the intact ATP synthase dimer from *Trypanosoma brucei* in ten  
23 different rotational states. The model consists of 25 subunits, including nine lineage-specific,  
24 as well as 36 lipids. The rotary mechanism is influenced by the divergent peripheral stalk,  
25 conferring a greater conformational flexibility. Proton transfer in the luminal half-channel  
26 occurs via a chain of five ordered water molecules. The dimerization interface is formed by  
27 subunit-g that is critical for interactions but not for the catalytic activity. Although overall  
28 dimer architecture varies among eukaryotes, we find that subunit-g together with subunit-e  
29 form an ancestral oligomerization motif, which is shared between the trypanosomal and  
30 mammalian lineages. Therefore, our data defines the subunit-g/e module as a structural  
31 component determining ATP synthase oligomeric assemblies.

34 Mitochondrial ATP synthase consists of the soluble F<sub>1</sub> and membrane-bound F<sub>o</sub> subcomplexes,  
35 and occurs in dimers that assemble into oligomers to induce the formation of inner-membrane  
36 folds, called cristae. The cristae are the sites for oxidative phosphorylation and energy  
37 conversion in eukaryotic cells. Dissociation of ATP synthase dimers into monomers results in  
38 the loss of native cristae architecture and impairs mitochondrial function<sup>1,2</sup>. While cristae  
39 morphology varies substantially between organisms from different lineages, ranging from flat  
40 lamellar in opisthokonts to coiled tubular in ciliates and discoidal in euglenozoans<sup>3</sup>, the  
41 mitochondrial ATP synthase dimers represent a universal occurrence to maintain the  
42 membrane shape<sup>4</sup>.

43 ATP synthase dimers of variable size and architecture, classified into types I to IV have  
44 recently been resolved by high-resolution cryo-EM studies. In the structure of the type-I ATP  
45 synthase dimer from mammals, the monomers are only weakly associated<sup>5,6</sup>, and in yeast  
46 insertions in the membrane subunits form tighter contacts<sup>7</sup>. The structure of the type-II ATP  
47 synthase dimer from the alga *Polytomella* sp. showed that the dimer interface is formed by  
48 phylum-specific components<sup>8</sup>. The type-III ATP synthase dimer from the ciliate *Tetrahymena*  
49 thermophila is characterized by parallel rotary axes, and a substoichiometric subunit, as well  
50 as multiple lipids were identified at the dimer interface, while additional protein components  
51 that tie the monomers together are distributed between the matrix, transmembrane, and luminal  
52 regions<sup>9</sup>. The structure of the type-IV ATP synthase with native lipids from *Euglena gracilis*  
53 also showed that specific protein-lipid interactions contribute to the dimerization, and that the  
54 central and peripheral stalks interact with each other directly<sup>10</sup>. Finally, a unique apicomplexan  
55 ATP synthase dimerizes via 11 parasite-specific components that contribute ~7000 Å<sup>2</sup> buried  
56 surface area<sup>11</sup>, and unlike all other ATP synthases, that assemble into rows, it associates in  
57 higher oligomeric states of pentagonal pyramids in the curved apical membrane regions.  
58 Together, the available structural data suggest a diversity of oligomerization, and it remains  
59 unknown whether common elements mediating these interactions exist or whether  
60 dimerization of ATP synthase occurred independently and multiple times in evolution<sup>4</sup>.

61 The ATP synthase of *Trypanosoma brucei*, a representative of kinetoplastids and an established  
62 medically important model organism causing the sleeping sickness, is highly divergent,  
63 exemplified by the pyramid-shaped F<sub>1</sub> head containing a phylum specific subunit<sup>12,13</sup>. The  
64 dimers are sensitive to the lack of cardiolipin<sup>14</sup> and form short left-handed helical segments  
65 that extend across the membrane ridge of the discoidal cristae<sup>15</sup>. Uniquely among aerobic  
66 eukaryotes, the mammalian life cycle stage of *T. brucei* utilizes the reverse mode of ATP  
67 synthase, using the enzyme as a proton pump to maintain mitochondrial membrane potential  
68 at the expense of ATP<sup>16,17</sup>. In contrast, the insect stages of the parasite employ the ATP-  
69 producing forward mode of the enzyme<sup>18,19</sup>.

70 Given the conservation of the core subunits, the different nature of oligomerization and the  
71 ability to test structural hypotheses biochemically, we reasoned that investigation of the *T.*  
72 *brucei* ATP synthase structure and function would provide the missing evolutionary link to  
73 understand how the monomers interact to form physiological dimers. Here, we address this  
74 question by combining structural, functional and evolutionary analysis of the *T. brucei* ATP  
75 synthase dimer.

76

## 77 Results

### 78 Cryo-EM structure of the *T. brucei* ATP synthase

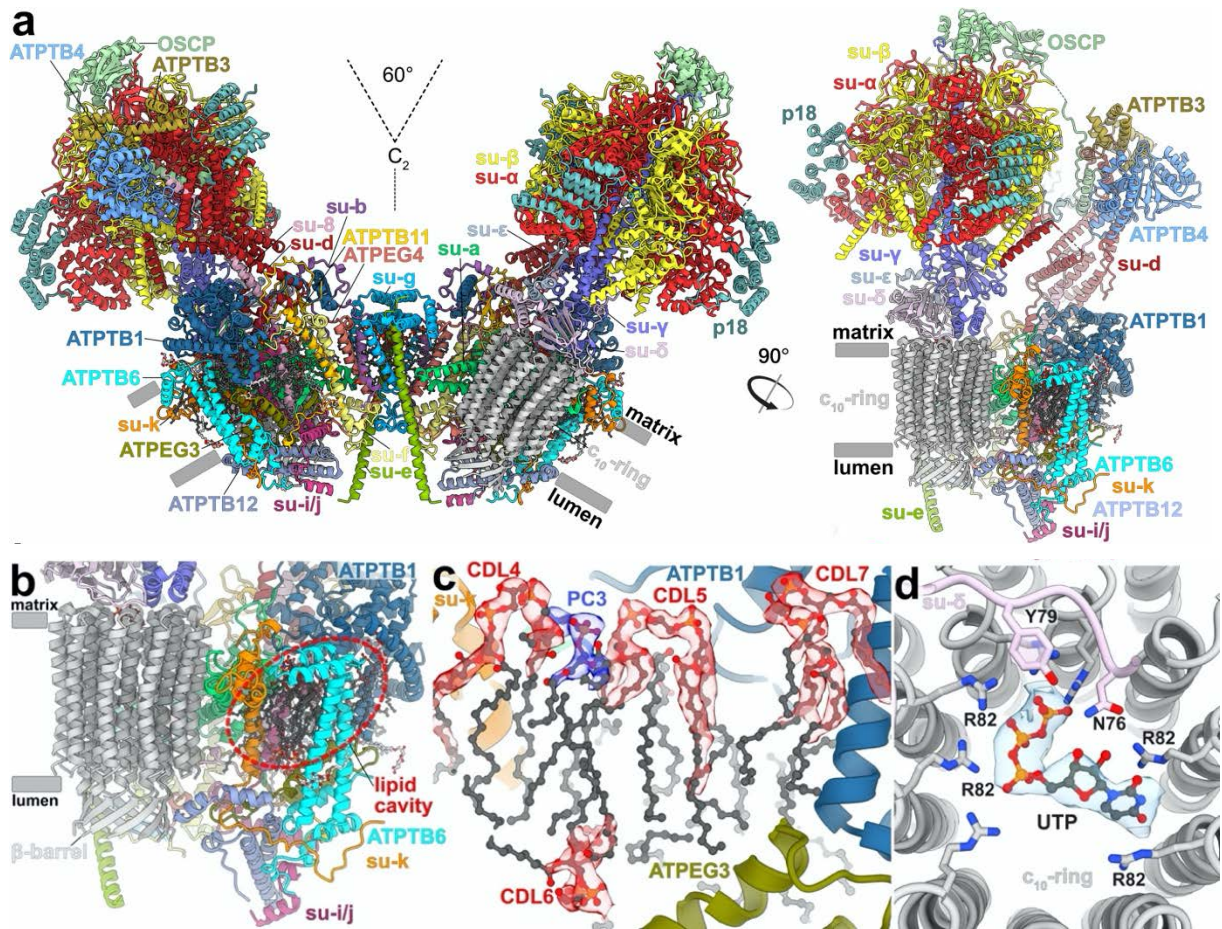
79 We purified ATP synthase dimers from cultured *T. brucei* procyclic trypomastigotes by affinity  
80 chromatography with a recombinant natural protein inhibitor TbIF<sub>1</sub><sup>20</sup>, and subjected the sample  
81 to cryo-EM analysis (Extended Data Fig. 1 and 2). Using masked refinements, maps were  
82 obtained for the membrane region, the rotor, and the peripheral stalk. To describe the  
83 conformational space of the *T. brucei* ATP synthase, we resolved ten distinct rotary substates,  
84 which were refined to 3.5-4.3 Å resolution. Finally, particles with both monomers in rotational  
85 state 1 were selected, and the consensus structure of the dimer was refined to 3.2 Å resolution  
86 (Extended Data Table 1, Extended Data Fig. 2).

87 Unlike the wide-angle architecture of dimers found in animals and fungi, the *T. brucei* ATP  
88 synthase displays an angle of 60° between the two F<sub>1</sub>/c-ring subcomplexes. The model of the  
89 *T. brucei* ATP synthase includes all 25 different subunits, nine of which are lineage-specific  
90 (Fig. 1a, Supplementary Video 1, Extended Data Fig. 3). We named the subunits according to  
91 the previously proposed nomenclature<sup>21-23</sup> (Extended Data Table 2). In addition, we identified  
92 and modeled 36 bound phospholipids, including 24 cardiolipins (Extended Data Fig. 4). Both  
93 detergents used during purification, n-dodecyl β-D-maltoside (β-DDM) and glyco-diosgenin  
94 (GDN) are also resolved in the periphery of the membrane region (Extended Data Fig. 5).

95 In the catalytic region, F<sub>1</sub> is augmented by three copies of subunit p18, each bound to subunit-  
96 α<sup>12,13</sup>. Our structure shows that p18 is involved in the unusual attachment of F<sub>1</sub> to the peripheral  
97 stalk. The membrane region includes eight conserved F<sub>o</sub> subunits (*b*, *d*, *f*, 8, *i/j*, *k*, *e*, and *g*)  
98 arranged around the central proton translocator subunit-*a*. We identified those subunits based  
99 on the structural similarity and matching topology to their yeast counterparts (Fig 2). For  
100 subunit-*b*, a single transmembrane helix superimposes well with bH1 from yeast and anchors  
101 the newly identified subunit-*e* and -*g* to the F<sub>o</sub> (Fig 2a); a long helix bH2, which constitutes the  
102 central part of the peripheral stalk in other organisms is absent in *T. brucei*. The sequence of  
103 this highly reduced subunit-*b* shows 18% identity and 40% similarity to *E. gracilis* subunit-  
104 *b*<sup>10</sup>, representing a diverged homolog (Extended Data Fig. 6). No alternative subunit-*b*<sup>24</sup> is  
105 found in our structure.

106 The membrane region contains a peripheral subcomplex, formed primarily by the phylum-  
107 specific ATPTB1,6,12 and ATPEG3 (Fig. 1b). It is separated from the conserved core by a  
108 membrane-intrinsic cavity, in which nine bound cardiolipins are resolved (Fig. 1c), and the  
109 C-terminus of ATPTB12 interacts with the luminal β-barrel of the c<sub>10</sub>-ring. In the cavity of the  
110 decameric c-ring near the matrix side, 10 Arg66<sub>c</sub> residues coordinate a ligand density, which  
111 is consistent with a pyrimidine ribonucleoside triphosphate (Fig. 1d). We assign this density as  
112 uridine-triphosphate (UTP), due to its large requirement in the mitochondrial RNA metabolism  
113 of African trypanosomes being a substrate for post-transcriptional RNA editing<sup>25</sup>, and addition  
114 of poly-uridine tails to gRNAs and rRNAs<sup>26,27</sup>, as well as due to low abundance of cytidine  
115 triphosphate (CTP)<sup>28</sup>. The nucleotide base is inserted between two Arg82<sub>c</sub> residues, whereas  
116 the triphosphate region is coordinated by another five Arg82<sub>c</sub> residues, with Tyr79<sub>δ</sub> and Asn76<sub>δ</sub>  
117 providing asymmetric coordination contacts. The presence of a nucleotide inside the c-ring is

118 surprising, given the recent reports of phospholipids inside the *c*-rings in mammals<sup>5,6</sup> and  
 119 ciliates<sup>9</sup>, indicating that a range of different ligands can provide structural scaffolding.

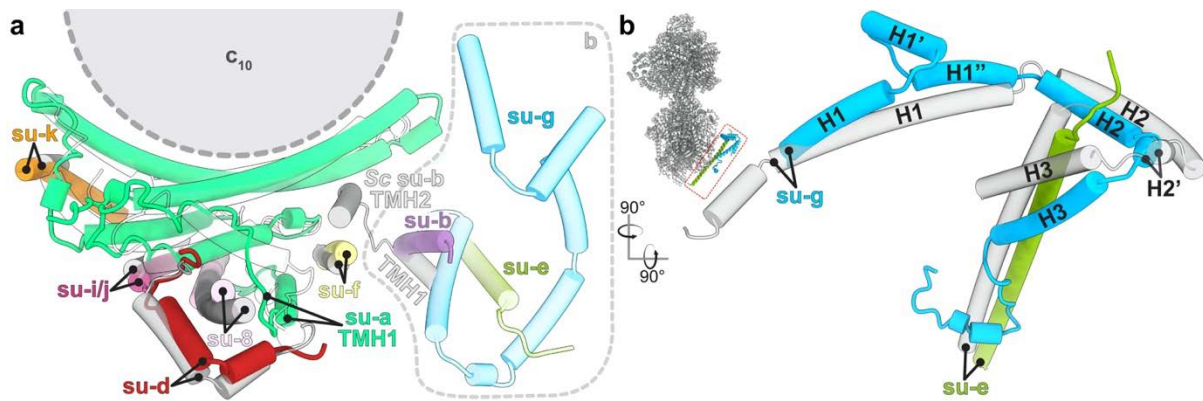


120

121

122 **Fig. 1: The *T. brucei* ATP synthase structure with lipids and ligands.**

123 **a**, Front and side views of the composite model with both monomers in rotational state 1. The  
 124 two F<sub>1</sub>/c<sub>10</sub>-ring complexes, each augmented by three copies of the phylum-specific p18 subunit,  
 125 are tied together at a 60°-angle. The membrane-bound F<sub>0</sub> region displays a unique architecture  
 126 and is composed of both conserved and phylum-specific subunits. **b**, Side view of the F<sub>0</sub> region  
 127 showing the luminal interaction of the ten-stranded β-barrel of the *c*-ring (grey) with ATPTB12  
 128 (pale blue). The lipid-filled peripheral F<sub>0</sub> cavity is indicated. **c**, Close-up view of the bound  
 129 lipids within the peripheral F<sub>0</sub> cavity with cryo-EM density shown. **d**, Top view into the  
 130 decameric *c*-ring with a bound pyrimidine ribonucleoside triphosphate, assigned as UTP. Map  
 131 density shown in transparent blue, interacting residues shown.



132

133 **Fig. 2: Identification of conserved F<sub>0</sub> subunits.**

134 **a**, Top view of the membrane region with *T. brucei* subunits (colored) overlaid with  
 135 *S. cerevisiae* structure (gray transparent). Close structural superposition and matching topology  
 136 allowed the assignment of conserved subunits based on matching topology and location.  
 137 **b**, Superposition of subunits-*e* and -*g* with their *S. cerevisiae* counterparts (PDB 6B2Z)  
 138 confirms their identity.

139

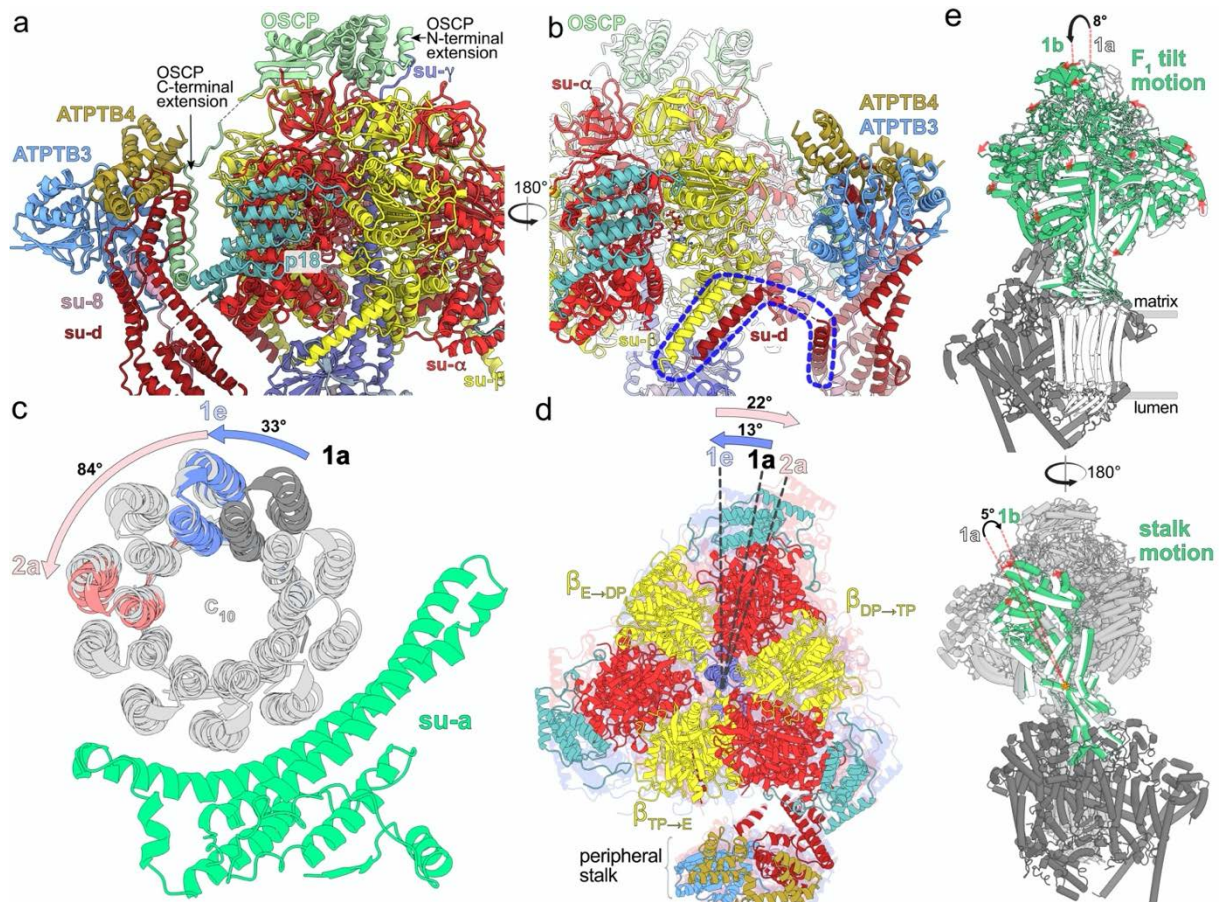
140 **Peripheral stalk flexibility and distinct rotational states**

141 The trypanosomal peripheral stalk displays a markedly different architecture compared to its  
 142 yeast and mammalian counterparts. In the opisthokont complexes, the peripheral stalk is  
 143 organized around the long *bH2*, which extends from the membrane ~15 nm into the matrix and  
 144 attaches to OSCP at the top of F<sub>1</sub><sup>5,7</sup>. By contrast, *T. brucei* lacks the canonical *bH2* and instead,  
 145 helices 5-7 of divergent subunit-*d* and the C-terminal helix of extended subunit-8 bind to a C-  
 146 terminal extension of OSCP at the apical part of the peripheral stalk (Fig. 3a). The interaction  
 147 between OSCP and subunit-*d* and -8 is stabilized by soluble ATPTB3 and ATPTB4. The  
 148 peripheral stalk is rooted to the membrane subcomplex by a transmembrane helix of subunit-  
 149 8, wrapped on the matrix side by helices 8-11 of subunit-*d*. Apart from the canonical contacts  
 150 at the top of F<sub>1</sub>, the peripheral stalk is attached to the F<sub>1</sub> via a euglenozoa-specific C-terminal  
 151 extension of OSCP, which contains a disordered linker and a terminal helix hairpin extending  
 152 between the F<sub>1</sub>-bound p18 and subunits -*d* and -8 of the peripheral stalk (Fig. 3a,  
 153 Supplementary Videos 2,3). Another interaction of F<sub>1</sub> with the peripheral stalk occurs between  
 154 the stacked C-terminal helices of subunit-β and -*d* (Fig. 3b), the latter of which structurally  
 155 belongs to F<sub>1</sub> and is connected to the peripheral stalk via a flexible linker.

156 To assess whether the unusual peripheral stalk architecture influences the rotary mechanism,  
 157 we analysed 10 classes representing different rotational states. The three main states (1-3) result  
 158 from a ~120° rotation of the central stalk subunit-γ, and we identified five (1a-1e), four (2a-2d)  
 159 and one (3) classes of the respective main states. The rotor positions of the rotational states 1a,  
 160 2a and 3 are related by steps of 117°, 136° and 107°, respectively. Throughout all the identified  
 161 substeps of the rotational state 1 (classes 1a to 1e) the rotor turns by ~33°, which corresponds  
 162 approximately to the advancement by one subunit-*c* of the  $c_{10}$ -ring. While rotating along with  
 163 the rotor, the F<sub>1</sub> headpiece lags behind, advancing by only ~13°. During the following transition  
 164 from 1e to 2a, the rotor advances by ~84°, whereas the F<sub>1</sub> headpiece rotates ~22° in the opposite  
 165 direction (Fig. 3c,d). This generates a counter-directional torque between the two motors,

166 which is consistent with a power-stroke mechanism. Albeit with small differences in step size,  
 167 this mechanism is consistent with a previous observation in the *Polytomella* ATP synthase<sup>8</sup>.  
 168 However, due to its large, rigid peripheral stalk, the *Polytomella* ATP synthase mainly displays  
 169 rotational substeps, whereas the *Trypanosoma* F<sub>1</sub> also displays a tilting motion of ~8° revealed  
 170 by rotary states 1 and 2 (Fig. 3e, Supplementary Video 2). The previously reported hinge  
 171 motion between the N- and C-terminal domains of OSCP<sup>8</sup> is not found in our structures,  
 172 instead, the conformational changes of the F<sub>1</sub>/c<sub>10</sub>-ring subcomplex are accommodated by a 5°  
 173 bending of the apical part of the peripheral stalk. (Fig. 3e, Supplementary Videos 2,3).  
 174 Together, the structural data indicate that the divergent peripheral stalk attachment confers  
 175 greater conformational flexibility to the *T. brucei* ATP synthase.

176



177

178 **Fig. 3: A divergent peripheral stalk allows high flexibility during rotary catalysis.** **a**, N-  
 179 terminal OSCP extension provides a permanent central stalk attachment, while the C-terminal  
 180 extension provides a phylum-specific attachment to the divergent peripheral stalk. **b**, The C-  
 181 terminal helices of subunits  $-\beta$  and  $-d$  provide a permanent F<sub>1</sub> attachment. **c**, Substeps of the  $c$ -  
 182 ring during transition from rotational state 1 to 2. **d**, F<sub>1</sub> motion accommodating steps shown in  
 183 (c). After advancing along with the rotor to state 1e, the F<sub>1</sub> rotates in the opposite direction  
 184 when transitioning to state 2a. **e**, Tilting motion of F<sub>1</sub> and accommodating bending of the  
 185 peripheral stalk.

186

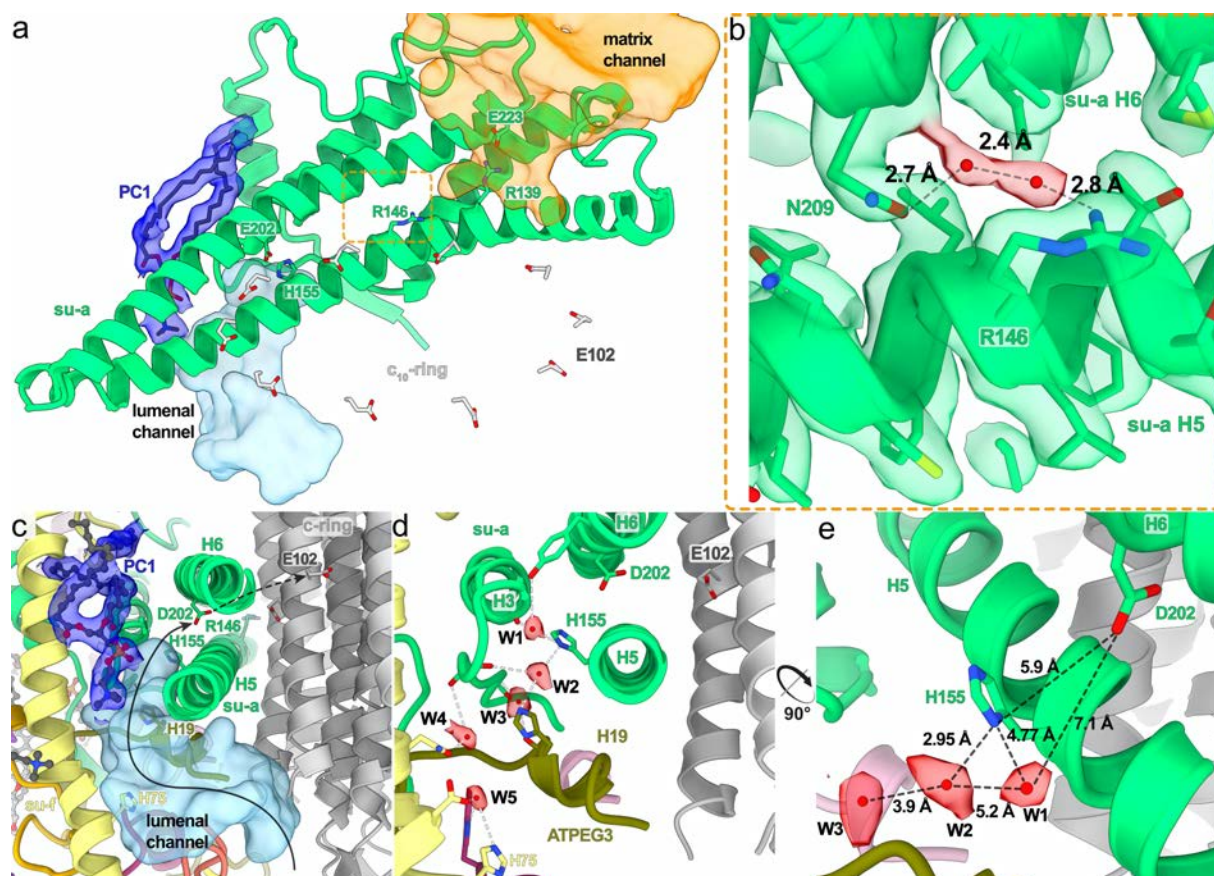
187

188 **Luminal proton half-channel is insulated by a lipid and contains ordered water molecules**

189 The mechanism of proton translocation involves sequential protonation of E102 of subunits-*c*,  
190 rotation of the *c*<sub>10</sub>-ring with neutralized E102*c* exposed to the phospholipid bilayer, and release  
191 of protons on the other side of the membrane. The sites of proton binding and release are  
192 separated by the conserved R146 contributed by the horizontal helix H5 of subunit-*a* and are  
193 accessible from the cristae lumen and mitochondrial matrix by aqueous half-channels (Fig. 4a).  
194 Together, R146 and the adjacent N209 coordinate a pair of water molecules in between helices  
195 H5 and H6 (Fig. 4b). A similar coordination has been observed in the *Polytomella* ATP  
196 synthase<sup>8</sup>. The coordination of water likely restricts the R146 to rotamers that extend towards  
197 the *c*-ring, with which it is thought to interact.

198 In our structure, the luminal half-channel is filled with a network of resolved water densities,  
199 ending in a chain of five ordered water molecules (W1-W5; Fig. 4c,d,e). The presence of  
200 ordered water molecules in the aqueous channel is consistent with a Grotthuss-type mechanism  
201 for proton transfer, which would not require long-distance diffusion of water molecules<sup>5</sup>.  
202 However, because some distances between the observed water molecules are too large for  
203 direct hydrogen bonding, proton transfer may involve both coordinated and disordered water  
204 molecules. The distance of 7 Å between the last resolved water (W1) and D202<sub>a</sub>, the conserved  
205 residue that is thought to transfer protons to the *c*-ring, is too long for direct proton transfer.  
206 Instead, it may occur via the adjacent H155<sub>a</sub>. Therefore, our structure resolves individual  
207 elements participating in proton transport (Fig. 4d,e).

208 The luminal proton half-channel in the mammalian<sup>5,6</sup> and apicomplexan<sup>11</sup> ATP synthase is  
209 lined by the transmembrane part of *bH2*, which is absent in *T. brucei*. Instead, the position of  
210 *bH2* is occupied by a fully ordered phosphatidylcholine in our structure (PC1; Fig. 4a,c).  
211 Therefore, a bound lipid replaces a proteinaceous element in the proton path.



212  
 213 **Fig. 4: The luminal half-channel contains ordered water molecules and is confined by an**  
 214 **F<sub>o</sub>-bound lipid.** **a**, Subunit-*a* (green) with the matrix (orange) and luminal (light blue)  
 215 channels, and an ordered phosphatidylcholine (PC1; blue). E102 of the *c*<sub>10</sub>-ring shown in grey.  
 216 **b**, Close-up view of the highly conserved R146<sub>a</sub> and N209<sub>a</sub>, which coordinate two water  
 217 molecules between helices H5-6<sub>a</sub>. **c**, Sideview of the luminal channel with proton pathway  
 218 (light blue) and confining phosphatidylcholine (blue). **d**, Chain of ordered water molecules in  
 219 the luminal channel. Distances between the W1-W5 (red) are 5.2, 3.9, 7.3 and 4.8 Å,  
 220 respectively. **e**, The ordered waters extend to H155<sub>a</sub>, which likely mediates the transfer of  
 221 protons to D202<sub>a</sub>.

222

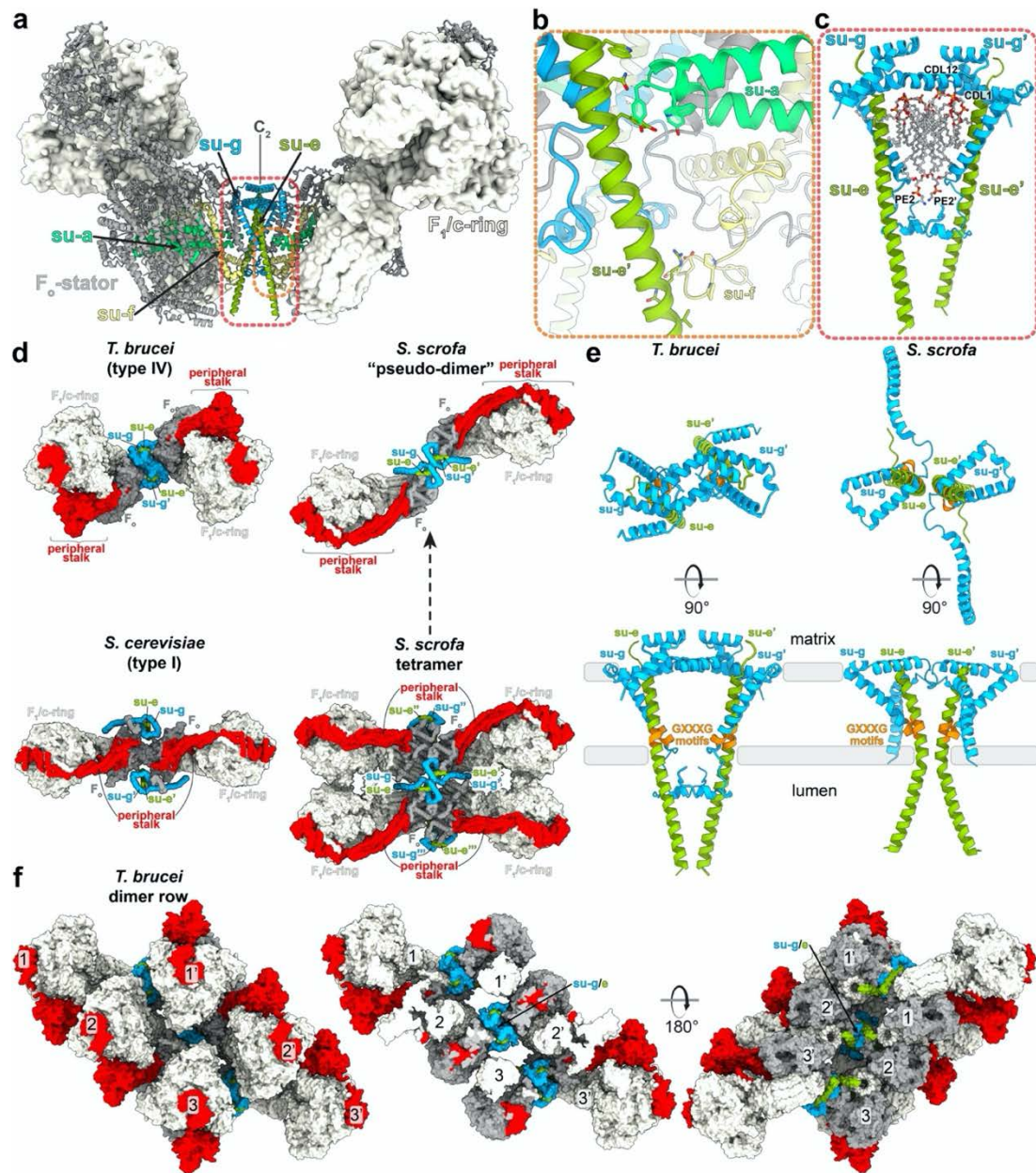
### 223 Subunit-g facilitates assembly of different ATP synthase oligomers

224 Despite sharing a set of conserved F<sub>o</sub> subunits, the *T. brucei* ATP synthase dimer displays a  
 225 markedly different dimer architecture compared to previously determined structures. First, its  
 226 dimerization interface of 3,600 Å<sup>2</sup> is smaller than that of the *E. gracilis* type-IV (10,000 Å<sup>2</sup>)  
 227 and the *T. thermophila* type-III ATP synthases (16,000 Å<sup>2</sup>). Second, unlike mammalian and  
 228 fungal ATP synthase, in which the peripheral stalks extend in the plane defined by the two  
 229 rotary axes, in our structure the monomers are rotated such that the peripheral stalks are offset  
 230 laterally on the opposite sides of the plane. Due to the rotated monomers, this architecture is  
 231 associated with a specific dimerization interface, where two subunit-g copies interact  
 232 homotypically on the C<sub>2</sub> symmetry axis (Fig. 5a, Supplementary Video 1). Both copies of H1-  
 233 2<sub>g</sub> extend horizontally along the matrix side of the membrane, clamping against each other  
 234 (Fig. 5c,e). This facilitates formation of contacts between an associated transmembrane helix

235 of subunit-*e* with the neighbouring monomer via subunit-*a*' in the membrane, and -*f*' in the  
236 lumen, thereby further contributing to the interface (Fig. 5b). Thus, the ATP synthase dimer is  
237 assembled via the subunit-*e/g* module. The C-terminal part of the subunit-*e* helix extends into  
238 the lumen, towards the ten-stranded  $\beta$ -barrel of the *c*-ring (Extended Data Fig. 7a). The terminal  
239 23 residues are disordered with poorly resolved density connecting to the detergent plug of the  
240 *c*-ring  $\beta$ -barrel (Extended Data Fig. 7b). This resembles the luminal C-terminus of subunit-*e*  
241 in the bovine structure<sup>5</sup>, indicating a conserved interaction with the *c*-ring.

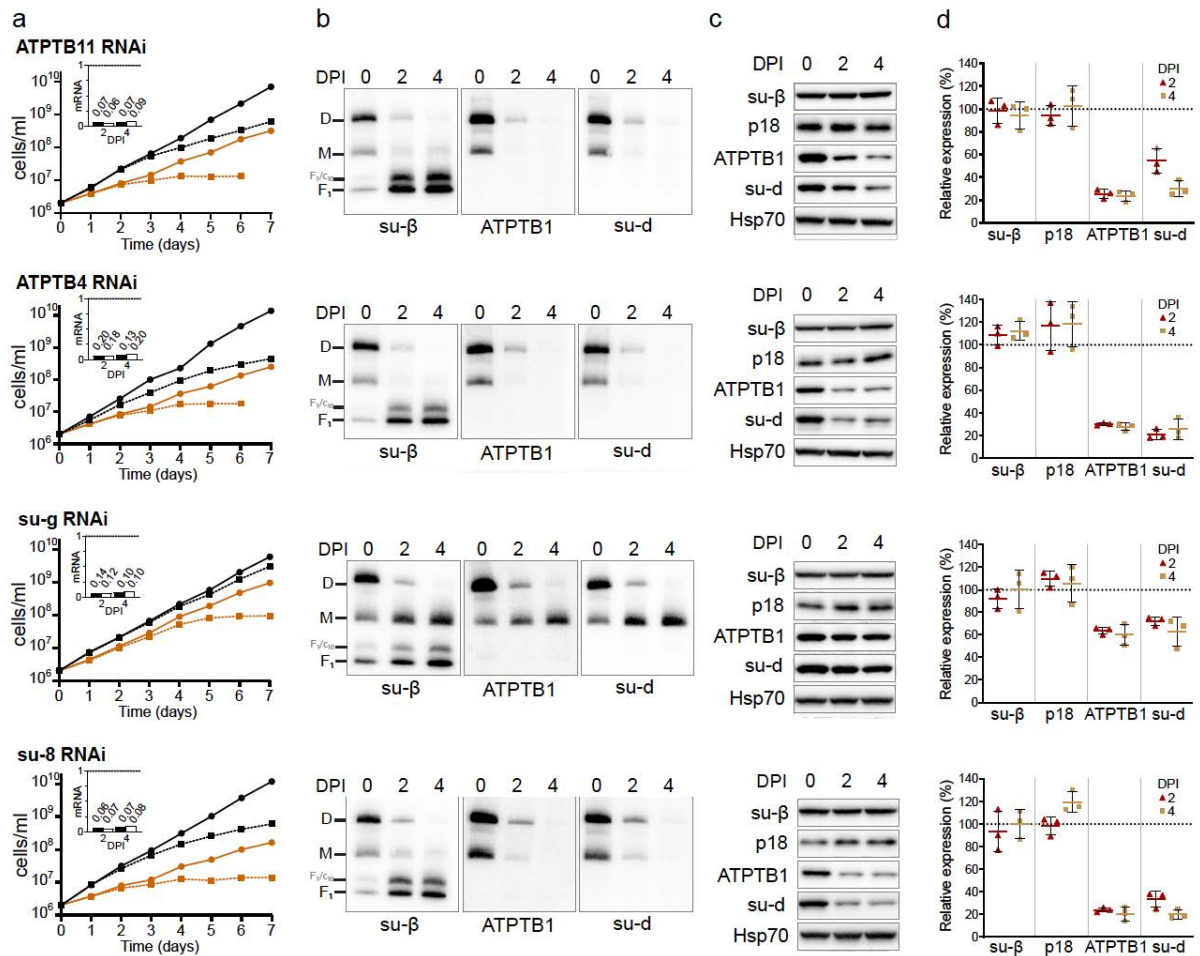
242 The *e/g* module is held together by four bound cardiolipins in the matrix leaflet, anchoring it  
243 to the remaining F<sub>o</sub> region (Fig. 5c). The head groups of the lipids are coordinated by polar and  
244 charged residues with their acyl chains filling a central cavity in the membrane region at the  
245 dimer interface (Fig 5c, Extended Data Fig. 4f). Cardiolipin binding has previously been  
246 reported to be obligatory for dimerization in secondary transporters<sup>29</sup> and the depletion of  
247 cardiolipin synthase resulted in reduced levels of ATP synthase in bloodstream  
248 trypanosomes<sup>14</sup>.

249 Interestingly, for yeasts, early blue native gel electrophoresis<sup>30</sup> and subtomogram averaging  
250 studies<sup>2</sup> suggested subunit-*g* as potentially dimer-mediating, however the *e/g* modules are  
251 located laterally opposed on either side of the dimer long axis, in the periphery of the complex,  
252 ~8.5 nm apart from each other. Because the *e/g* modules do not interact directly within the  
253 yeast ATP synthase dimer, they have been proposed to serve as membrane-bending elements,  
254 whereas the major dimer contacts are formed by subunit-*a* and -*i/j*<sup>7</sup>. In mammals, the *e/g*  
255 module occupies the same position as in yeasts, forming the interaction between two diagonal  
256 monomers in a tetramer<sup>5,6,31</sup>, as well as between parallel dimers<sup>32</sup>. The comparison with our  
257 structure shows that the overall organization of the intra-dimeric trypanosomal and inter-  
258 dimeric mammalian *e/g* module is structurally similar (Fig. 5d). Furthermore, kinetoplastid  
259 parasites and mammals share conserved GXXXG motifs in subunit-*e*<sup>33</sup> and -*g* (Extended Data  
260 Fig. 8), which allow close interaction of their transmembrane helices (Fig. 5e), providing  
261 further evidence for subunit homology. However, while the mammalian ATP synthase dimers  
262 are arranged perpendicularly to the long axis of their rows along the edge of cristae<sup>34</sup>, the  
263 *T. brucei* dimers on the rims of discoidal cristae are inclined ~45° to the row axis<sup>15</sup>. Therefore,  
264 the *e/g* module occupies equivalent positions in the rows of both evolutionary distant groups  
265 (Fig. 5f and reference 32).



266

267 **Fig. 5: The homotypic dimerization motif of subunit-g generates a conserved**  
 268 **oligomerization module.** a, Side view with dimerising subunits colored. b,c, The dimer  
 269 interface is constituted by (b) subunit-e' contacting subunit-a in the membrane and subunit-f  
 270 in the lumen, (c) subunits e and g from both monomers forming a subcomplex with bound  
 271 lipids. d, Subunit-g and -e form a dimerization motif in the trypanosomal (type-IV) ATP  
 272 synthase dimer (this study), the same structural element forms the oligomerization motif in the  
 273 porcine ATP synthase tetramer. The structural similarity of the pseudo-dimer (i.e., two  
 274 diagonal monomers from adjacent dimers) in the porcine structure with the trypanosomal dimer  
 275 suggests that type I and IV ATP synthase dimers have evolved through divergence from a  
 276 common ancestor. e, The dimeric subunit-e/g structures are conserved in pig (PDB 6ZNA) and  
 277 *T. brucei* (this work) and contain a conserved GXXXG motif (orange) mediating interaction of  
 278 transmembrane helices. f, Models of the ATP synthase dimers fitted into subtomogram  
 279 averages of short oligomers<sup>15</sup>: matrix view, left; cut-through, middle, lumenal view, right  
 280 (EMD-3560).



281

282

283

284

285

286

287

288

289

290

291

**Fig. 6: RNAi knockdown of subunit-g results in monomerization of ATP synthase. a,** Growth curves of non-induced (solid lines) and tetracycline-induced (dashed lines) RNAi cell lines grown in the presence (black) or absence (brown) of glucose. The insets show relative levels of the respective target mRNA at indicated days post-induction (DPI) normalized to the levels of 18S rRNA (black bars) or  $\beta$ -tubulin (white bars). **b,** Immunoblots of mitochondrial lysates from indicated RNAi cell lines resolved by BN-PAGE probed with antibodies against indicated ATP synthase subunits. **c,** Representative immunoblots of whole cell lysates from indicated RNAi cell lines probed with indicated antibodies. **d,** Quantification of three replicates of immunoblots in (c). Values were normalized to the signal of the loading control Hsp70 and to non-induced cells. Plots show means with standard deviations (SD).

## 292 **Subunit-g retains the dimer but is not essential for the catalytic monomer**

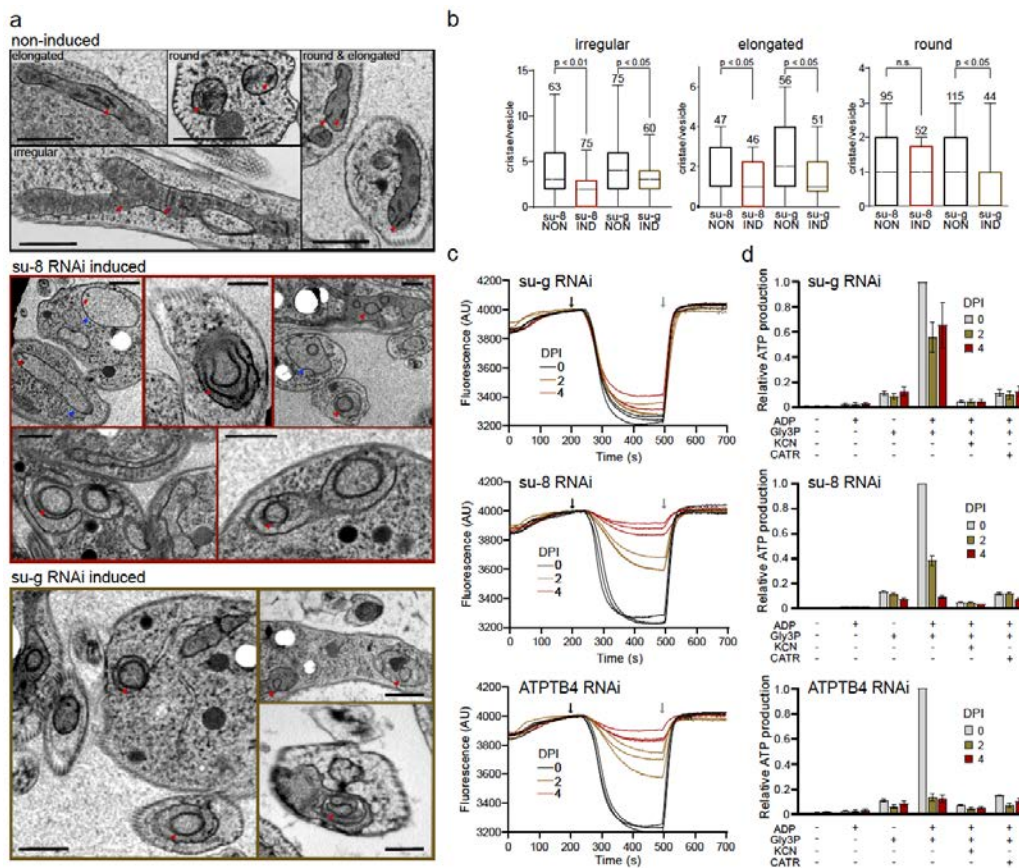
293 To validate structural insights, we knocked down each individual F<sub>o</sub> subunit by inducible RNA  
294 interference (RNAi). All target mRNAs dropped to 5-20 % of their original levels after two  
295 and four days of induction (Fig. 6a and Extended Data Fig. 9a). Western blot analysis of whole-  
296 cell lysates resolved by denaturing electrophoresis revealed decreased levels of F<sub>o</sub> subunits  
297 ATPB1 and *-d* suggesting that the integrity of the F<sub>o</sub> moiety depends on the presence of other  
298 F<sub>o</sub> subunits (Fig. 6c,d). Immunoblotting of mitochondrial complexes resolved by blue native  
299 polyacrylamide gel electrophoresis (BN-PAGE) with antibodies against F<sub>1</sub> and F<sub>o</sub> subunits  
300 revealed a strong decrease or nearly complete loss of dimeric and monomeric forms of ATP  
301 synthases four days after induction of RNAi of most subunits (*b, e, f, i/j, k, 8, ATPTB3,*  
302 *ATPTB4, ATPTB6, ATPTB11, ATPTB12, ATPEG3 and ATPEG4*), documenting an  
303 increased instability of the enzyme or defects in its assembly. Simultaneous accumulation in  
304 F<sub>1</sub>-ATPase, as observed by BN-PAGE, demonstrated that the catalytic moiety remains intact  
305 after the disruption of the peripheral stalk or the membrane subcomplex (Fig. 6b,c,d and  
306 Extended Data Fig. 9b).

307 In contrast to the other targeted F<sub>o</sub> subunits, the downregulation of subunit-g with RNAi  
308 resulted in a specific loss of dimeric complexes with concomitant accumulation of monomers  
309 (Fig. 6b), indicating that it is required for dimerization, but not for the assembly and stability  
310 of the monomeric F<sub>1</sub>F<sub>o</sub> ATP synthase units. Transmission electron microscopy of thin cell  
311 sections revealed that the ATP synthase monomerization in the subunit-g<sup>RNAi</sup> cell line had the  
312 same effect on mitochondrial ultrastructure as nearly complete loss of monomers and dimers  
313 upon knockdown of subunit-8. Both cell lines exhibited decreased cristae counts and aberrant  
314 cristae morphology (Fig. 7a,b), including the appearance of round shapes reminiscent of  
315 structures detected upon deletion of subunit-g or *-e* in *Saccharomyces cerevisiae*<sup>1</sup>. These results  
316 indicate that monomerization prevents the trypanosomal ATP synthase from assembling into  
317 short helical rows on the rims of the discoidal cristae<sup>15</sup>, as has been reported for impaired  
318 oligomerization in counterparts from other eukaryotes<sup>2,35</sup>.

319 Despite the altered mitochondrial ultrastructure, the subunit-g<sup>RNAi</sup> cells showed only a very  
320 mild growth phenotype, in contrast to all other RNAi cell lines that exhibited steadily slowed  
321 growth from day three to four after the RNAi induction (Fig. 7a, Extended Data Fig. 9a). This  
322 is consistent with the growth defects observed after the ablation of F<sub>o</sub> subunit ATPTB1<sup>19</sup> and  
323 F<sub>1</sub> subunits- $\alpha$  and p18<sup>12</sup>. Thus, the monomerization of ATP synthase upon subunit-g ablation  
324 had only a negligible effect on the fitness of trypanosomes cultured in glucose-rich medium,  
325 in which ATP production by substrate level phosphorylation partially compensates for  
326 compromised oxidative phosphorylation<sup>36</sup>.

327 Measurement of oligomycin-sensitive ATP-dependent mitochondrial membrane polarization  
328 by safranin O assay in permeabilized cells showed that the proton pumping activity of the ATP  
329 synthase in the induced subunit-g<sup>RNAi</sup> cells is negligibly affected, demonstrating that the  
330 monomerized enzyme is catalytically functional. By contrast, RNAi downregulation of  
331 subunit-8, ATPTB4 and ATPTB11, and ATPTB1 resulted in a strong decline of the  
332 mitochondrial membrane polarization capacity, consistent with the loss of both monomeric and  
333 dimeric ATP synthase forms (Fig. 7c). Accordingly, knockdown of the same subunits resulted  
334 in inability to produce ATP by oxidative phosphorylation (Fig. 7d). However, upon subunit-g

335 ablation the ATP production was affected only partially, confirming that the monomerized  
 336 ATP synthase remains catalytically active. The ~50 % drop in ATP production of subunit-g<sup>RNAi</sup>  
 337 cells can be attributed to the decreased oxidative phosphorylation efficiency due to the  
 338 impaired cristae morphology. Indeed, when cells were cultured in the absence of glucose,  
 339 enforcing the need for oxidative phosphorylation, knockdown of subunit-g results in a growth  
 340 arrest, albeit one to two days later than knockdown of all other tested subunits (Fig. 6a). The  
 341 data show that dimerization is critical when oxidative phosphorylation is the predominant  
 342 source of ATP.



343  
 344 **Fig. 7: Monomerization of ATP synthase by subunit-g knockdown results in aberrant**  
 345 **mitochondrial ultrastructure but does not abolish catalytic activity.** **a**, Transmission  
 346 electron micrographs of sections of non-induced or 4 days induced RNAi cell lines.  
 347 Mitochondrial membranes and cristae are marked with blue and red arrowheads, respectively.  
 348 Top panel shows examples of irregular, elongated and round cross-sections of mitochondria  
 349 quantified in (b). **b**, Cristae numbers per vesicle from indicated induced (IND) or non-induced  
 350 (NON) cell lines counted separately in irregular, elongated and round mitochondrial cross-  
 351 section. Boxes and whiskers show 25<sup>th</sup> to 75<sup>th</sup> and 5<sup>th</sup> to 95<sup>th</sup> percentiles, respectively. The  
 352 numbers of analysed cross-sections are indicated for each data point. Unpaired t-test, p-values  
 353 are shown. **c**, Mitochondrial membrane polarization capacity of non-induced or RNAi-induced  
 354 cell lines two and four DPI measured by Safranin O. Black and gray arrow indicate addition  
 355 of ATP and oligomycin, respectively. **d**, ATP production in permeabilized non-induced (0) or  
 356 RNAi-induced cells 2 and 4 DPI in the presence of indicated substrates and inhibitors. Error  
 357 bars represent SD of three replicates. *Gly3P*, DL-glycerol phosphate; *KCN*, potassium cyanide;  
 358 *CATR*, carboxyatractyloside

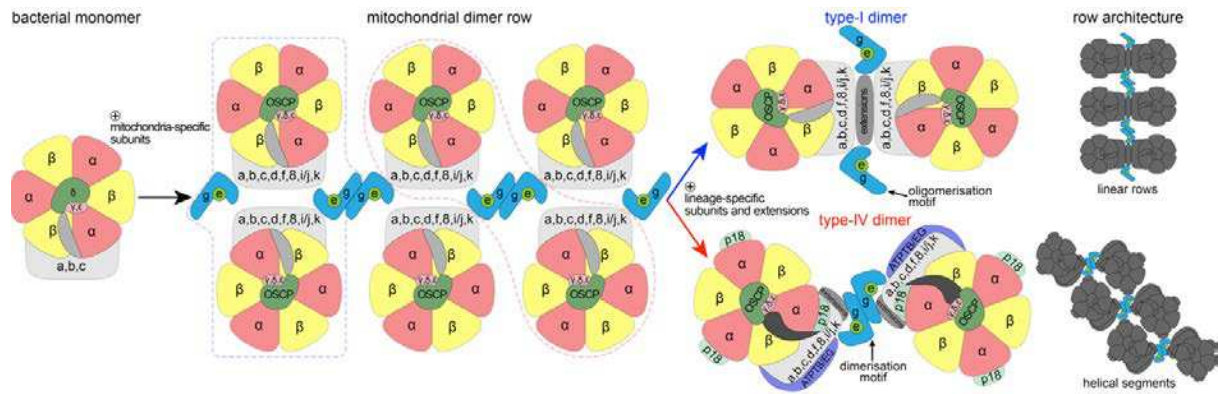
## 359 Discussion

360 Our structure of the mitochondrial ATP synthase dimer from the mammalian parasite *T. brucei*  
361 offers new insight into the mechanism of membrane shaping, rotary catalysis, and proton  
362 transfer. Considering that trypanosomes belong to an evolutionarily divergent group of  
363 Kinetoplastida, the ATP synthase dimer has several interesting features that differ from other  
364 dimer structures. The subunit-*b* found in bacterial and other mitochondrial F-type ATP  
365 synthases appears to be highly reduced to a single transmembrane helix *bH1*. The long *bH2*,  
366 which constitutes the central part of the peripheral stalk in other organisms, and is also involved  
367 in the composition of the luminal proton half-channel, is completely absent in *T. brucei*.  
368 Interestingly, the position of *bH2* in the proton half channel is occupied by a fully ordered  
369 phosphatidylcholine molecule that replaces a well-conserved proteinaceous element in the  
370 proton path. Lack of the canonical *bH2* also affects composition of the peripheral stalk in which  
371 the divergent subunit-*d* and subunit-*8* binds directly to a C-terminal extension of OSCP,  
372 indicating a remodeled peripheral stalk architecture. The peripheral stalk contacts the  $F_1$   
373 headpiece at several positions conferring greater conformational flexibility to the ATP  
374 synthase.

375 Using the structural and functional data, we also identified a conserved structural element of  
376 the ATP synthase that is responsible for its multimerization. Particularly, subunit-*g* is required  
377 for the dimerization, but dispensable for the assembly of the  $F_1F_0$  monomers. Although the  
378 monomerized enzyme is catalytically competent, the inability to form dimers results in  
379 defective cristae structure, and consequently leads to compromised oxidative phosphorylation  
380 and cease of proliferation. The cristae-shaping properties of mitochondrial ATP synthase  
381 dimers are critical for sufficient ATP production by oxidative phosphorylation, but not for other  
382 mitochondrial functions, as demonstrated by the lack of growth phenotype of subunit-*g*<sup>RNAi</sup>  
383 cells in the presence of glucose. Thus, trypanosomal subunit-*g* depletion strain represents an  
384 experimental tool to assess the roles of the enzyme's primary catalytic function and  
385 mitochondria-specific membrane-shaping activity, highlighting the importance of the latter for  
386 oxidative phosphorylation.

387 Based on our data and previously published structures, we propose an ancestral state with  
388 double rows of ATP synthase monomers connected by *e/g* modules longitudinally and by other  
389  $F_0$  subunits transversally. During the course of evolution, different pairs of adjacent ATP  
390 synthase monomer units formed stable dimers in individual lineages (Fig. 8). This gave rise to  
391 the highly divergent type-I and type-IV ATP synthase dimers with subunit-*e/g* modules serving  
392 either as oligomerization or dimerization motives, respectively. Because trypanosomes belong  
393 to the deep-branching eukaryotic supergroup Discoba, the proposed arrangement might have  
394 been present in the last eukaryotic common ancestor. Although sequence similarity of subunit-*g*  
395 is low and restricted to the single transmembrane helix, we found homologs of subunit-*g* in  
396 addition to Opisthokonta and Discoba also in Archaeplastida and Amoebozoa, which represent  
397 other eukaryotic supergroups, thus supporting the ancestral role in oligomerization (Extended  
398 Data Fig. 8). Taken together, our analysis reveals that mitochondrial ATP synthases that  
399 display markedly diverged architecture share the ancestral structural module that promotes  
400 oligomerization.

401



402

403 **Fig. 8: The subunit-*e/g* module is an ancestral oligomerization motif of ATP synthase.**  
 404 Schematic model of the evolution of type-I and IV ATP synthases. Mitochondrial ATP  
 405 synthases are derived from a monomeric complex of proteobacterial origin. In a mitochondrial  
 406 ancestor, acquisition of mitochondria-specific subunits, including the subunit-*e/g* module  
 407 resulted in the assembly of ATP synthase double rows, the structural basis for cristae  
 408 biogenesis. Through divergence, different ATP synthase architectures evolved, with the  
 409 subunit-*e/g* module functioning as an oligomerization (type I) or dimerization (type IV) motif,  
 410 resulting in distinct row assemblies between mitochondrial lineages.

411

## 412 **Materials and Methods**

### 413 Cell culture and isolation of mitochondria

414 *T. brucei* procyclic strains were cultured in SDM-79 medium supplemented with 10% (v/v)  
 415 fetal bovine serum. For growth curves in glucose-free conditions, cells were grown in SDM-  
 416 80 medium with 10 % dialysed FBS. RNAi cell lines were grown in presence of 2.5  $\mu\text{g/ml}$   
 417 phleomycin and 1  $\mu\text{g/ml}$  puromycin. For ATP synthase purification, mitochondria were  
 418 isolated from the Lister strain 427. Typically,  $1.5 \times 10^{11}$  cells were harvested, washed in 20 mM  
 419 sodium phosphate buffer pH 7.9 with 150 mM NaCl and 20 mM glucose, resuspended in  
 420 hypotonic buffer 1 mM Tris-HCl pH 8.0, 1 mM EDTA, and disrupted by 10 strokes in a 40-ml  
 421 Dounce homogenizer. The lysis was stopped by immediate addition of sucrose to 0.25 M.  
 422 Crude mitochondria were pelleted (15 min at 16,000 xg, 4°C), resuspended in 20 mM Tris-  
 423 HCl pH 8.0, 250 mM sucrose, 5 mM MgCl<sub>2</sub>, 0.3 mM CaCl<sub>2</sub> and treated with 5  $\mu\text{g/ml}$  DNase I.  
 424 After 60 min on ice, one volume of the STE buffer (20 mM Tris-HCl pH 8.0, 250 mM sucrose,  
 425 2 mM EDTA) was added and mitochondria were pelleted (15 min at 16000 xg, 4°C). The pellet  
 426 was resuspended in 60% (v/v) Percoll in STE and loaded on six linear 10-35% Percoll gradients  
 427 in STE in polycarbonate tubes for SW28 rotor (Beckman). Gradients were centrifuged for 1 h  
 428 at 24,000 rpm, 4°C. The middle phase containing mitochondrial vesicles (15-20 ml per tube)  
 429 was collected, washed four times in the STE buffer, and pellets were snap-frozen in liquid  
 430 nitrogen and stored at -80°C.

431

### 432 Plasmid construction and generation of RNAi cell lines

433 To downregulate ATP synthase subunits by RNAi, DNA fragments corresponding to  
 434 individual target sequences were amplified by PCR from Lister 427 strain genomic DNA using

435 forward and reverse primers extended with restriction sites *XhoI*&*KpnI* and *XbaI*&*BamHI*,  
436 respectively (Extended Data Table 3). Each fragment was inserted into the multiple cloning  
437 sites 1 and 2 of pAZ0055 vector, derived from pRP<sup>HYG-iSL</sup> (courtesy of Sam Alford) by  
438 replacement of hygromycin resistance gene with phleomycin resistance gene, with restriction  
439 enzymes *KpnI/BamHI* and *XhoI/XbaI*, respectively. Resulting constructs with tetracycline  
440 inducible T7 polymerase driven RNAi cassettes were linearized with *NotI* and transfected into  
441 a cell line derived from the Lister strain 427 by integration of the SmOx construct for  
442 expression of T7 polymerase and the tetracycline repressor<sup>37</sup> into the  $\beta$ -tubulin locus. RNAi  
443 was induced in selected semi-clonal populations by addition of 1  $\mu$ g/ml tetracycline and the  
444 downregulation of target mRNAs was verified by quantitative RT-PCR 2 and 4 days post  
445 induction. The total RNA isolated by an RNeasy Mini Kit (Qiagen) was treated with 2  $\mu$ g of  
446 DNase I, and then reverse transcribed to cDNA with TaqMan Reverse Transcription kit  
447 (Applied Biosciences). qPCR reactions were set with LightCycler 480 SYBR Green I Master  
448 mix (Roche), 2  $\mu$ l of cDNA and 0.3  $\mu$ M primers (Extended Data Table 3), and run on  
449 LightCycler 480 (Roche). Relative expression of target genes was calculated using  $-\Delta\Delta C_t$   
450 method with 18S rRNA or  $\beta$ -tubulin as endogenous reference genes and normalized to  
451 noninduced cells.

452

#### 453 Denaturing and blue native polyacrylamide electrophoresis and immunoblotting

454 Whole cell lysates for denaturing sodium dodecyl sulphate polyacrylamide electrophoresis  
455 (SDS-PAGE) were prepared from cells resuspended in PBS buffer (10 mM phosphate buffer,  
456 130 mM NaCl, pH 7.3) by addition of 3x Laemmli buffer (150 mM Tris pH 6.8, 300 mM 1,4-  
457 dithiothreitol, 6% (w/v) SDS, 30% (w/v) glycerol, 0.02% (w/v) bromophenol blue) to final  
458 concentration of  $1 \times 10^7$  cells in 30  $\mu$ l. The lysates were boiled at 97°C for 10 min and stored at  
459 -20°C. For immunoblotting, lysates from  $3 \times 10^6$  cells were separated on 4-20 % gradient Tris-  
460 glycine polyacrylamide gels (BioRad 4568094), electroblotted onto a PVDF membrane (Pierce  
461 88518), and probed with respective antibodies (Extended Data Table 4). Membranes were  
462 incubated with the Clarity Western ECL substrate (BioRad 1705060EM) and  
463 chemiluminescence was detected on a ChemiDoc instrument (BioRad). Band intensities were  
464 quantified densitometrically using the ImageLab software. The levels of individual subunits  
465 were normalized to the signal of mtHsp70.

466 Blue native PAGE (BN-PAGE) was performed as described earlier<sup>12</sup> with following  
467 modifications. Crude mitochondrial vesicles from  $2.5 \times 10^8$  cells were resuspended in 40  $\mu$ l of  
468 Solubilization buffer A (2 mM  $\epsilon$ -aminocaproic acid (ACA), 1 mM EDTA, 50 mM NaCl, 50  
469 mM Bis-Tris/HCl, pH 7.0) and solubilized with 2% (w/v) dodecylmaltoside ( $\beta$ -DDM) for 1 h  
470 on ice. Lysates were cleared at 16,000 g for 30 min at 4°C and their protein concentration was  
471 estimated using bicinchoninic acid assay. For each time point, a volume of mitochondrial lysate  
472 corresponding to 4  $\mu$ g of total protein was mixed with 1.5  $\mu$ l of loading dye (500 mM ACA,  
473 5% (w/v) Coomassie Brilliant Blue G-250) and 5% (w/v) glycerol and with 1 M ACA until a  
474 final volume of 20  $\mu$ l/well, and resolved on a native PAGE 3-12% Bis-Tris gel (Invitrogen).  
475 After the electrophoresis (3 h, 140 V, 4°C), proteins were transferred by electroblotting onto a

476 PVDF membrane (2 h, 100 V, 4°C, stirring), followed by immunodetection with an appropriate  
477 antibody (Extended Data Table 4).

478

#### 479 Mitochondrial membrane polarization measurement

480 The capacity to polarize mitochondrial membrane was determined fluorometrically employing  
481 safranin O dye (Sigma S2255) in permeabilized cells. For each sample,  $2 \times 10^7$  cells were  
482 harvested and washed with ANT buffer (8 mM KCl, 110 mM K-gluconate, 10 mM NaCl, 10  
483 mM free-acid Hepes, 10 mM  $K_2HPO_4$ , 0.015 mM EGTA potassium salt, 10 mM mannitol, 0.5  
484 mg/ml fatty acid-free BSA, 1.5 mM  $MgCl_2$ , pH 7.25). The cells were permeabilized by 8  $\mu$ M  
485 digitonin in 2 ml of ANT buffer containing 5  $\mu$ M safranin O. Fluorescence was recorded for  
486 700 s in a Hitachi F-7100 spectrofluorimeter (Hitachi High Technologies) at a 5-Hz acquisition  
487 rate, using 495 nm and 585 nm excitation and emission wavelengths, respectively. 1 mM ATP  
488 (PanReac AppliChem A1348,0025) and 10  $\mu$ g/ml oligomycin (Sigma O4876) were added after  
489 230 s and 500 s, respectively. Final addition of the uncoupler SF 6847 (250 nM; Enzo Life  
490 Sciences BML-EI215-0050) served as a control for maximal depolarization. All experiments  
491 were performed at room temperature and constant stirring.

492

#### 493 ATP production assay

494 ATP production in digitonin-isolated mitochondria was performed as described previously<sup>38</sup>.  
495 Briefly,  $1 \times 10^8$  cells per time point were lysed in SoTE buffer (600 mM sorbitol, 2 mM EDTA,  
496 20 mM Tris-HCl, pH 7.75) containing 0.015% (w/v) digitonin for 5 min on ice. After  
497 centrifugation (3 min, 4,000 g, 4°C), the soluble cytosolic fraction was discarded and the  
498 organellar pellet was resuspended in 75  $\mu$ l of ATP production assay buffer (600 mM sorbitol,  
499 10 mM  $MgSO_4$ , 15 mM potassium phosphate buffer pH 7.4, 20 mM Tris-HCl pH 7.4, 2.5  
500 mg/ml fatty acid-free BSA). ATP production was induced by addition of 20 mM DL-glycerol  
501 phosphate (sodium salt) and 67  $\mu$ M ADP. Control samples were preincubated with the  
502 inhibitors potassium cyanide (1 mM) and carboxyatractyloside (6.5  $\mu$ M) for 10 min at room  
503 temperature. After 30 min at room temperature, the reaction was stopped by addition of 1.5  $\mu$ l  
504 of 70% perchloric acid. The concentration of ATP was estimated using the Roche ATP  
505 Bioluminescence Assay Kit HS II in a Tecan Spark plate reader. The luminescence values of  
506 the RNAi induced samples were normalized to that of the corresponding noninduced sample.

507

#### 508 Thin sectioning and transmission electron microscopy

509 The samples were centrifuged and pellet was transferred to the specimen carriers which were  
510 completed with 20% BSA and immediately frozen using high pressure freezer Leica EM ICE  
511 (Leica Microsystems). Freeze substitution was performed in the presence of 2% osmium  
512 tetroxide diluted in 100% acetone at -90°C. After 96 h, specimens were warmed to -20°C at a  
513 slope 5 °C/h. After the next 24 h, the temperature was increased to 3°C (3°C/h). At room  
514 temperature, samples were washed in acetone and infiltrated with 25%, 50%, 75%  
515 acetone/resin EMBED 812 (EMS) mixture 1 h at each step. Finally, samples were infiltrated in  
516 100% resin and polymerized at 60°C for 48h. Ultrathin sections (70 nm) were cut using a

517 diamond knife, placed on copper grids and stained with uranyl acetate and lead citrate. TEM  
518 micrographs were taken with Mega View III camera (SIS) using a JEOL 1010 TEM operating  
519 at an accelerating voltage of 80 kV.

520

#### 521 Purification of *T. brucei* ATP synthase dimers

522 Mitochondria from  $3 \times 10^{11}$  cells were lysed by 1 % (w/v)  $\beta$ -DDM in 60 ml of 20 mM Bis-tris  
523 propane pH 8.0 with 10 % glycerol and EDTA-free Complete protease inhibitors (Roche) for  
524 20 min at 4°C. The lysate was cleared by centrifugation at 30,000 xg for 20 min at 4°C and  
525 adjusted to pH 6.8 by drop-wise addition of 1 M 3-(N-morpholino) propanesulfonic acid pH  
526 5.9. Recombinant TbIF<sub>1</sub> without dimerization region, whose affinity to F<sub>1</sub>-ATPase was  
527 increased by N-terminal truncation and substitution of tyrosine 36 with tryptophan<sup>20</sup>, with a C-  
528 terminal glutathione S-transferase (GST) tag (TbIF<sub>1</sub>(9-64)-Y36W-GST) was added in  
529 approximately 10-fold molar excess over the estimated content of ATP synthase. Binding of  
530 TbIF<sub>1</sub> was facilitated by addition of neutralized 2 mM ATP with 4 mM magnesium sulphate.  
531 After 5 min, sodium chloride was added to 100 mM, the lysate was filtered through a 0.2  $\mu$ m  
532 syringe filter and immediately loaded on 5 ml GSTrap HP column (Cytiva) equilibrated in 20  
533 mM Bis-Tris-Propane pH 6.8 binding buffer containing 0.1 % (w/v) glyco-diosgenin (GDN;  
534 Avanti Polar Lipids), 10 % (v/v) glycerol, 100 mM sodium chloride, 1 mM tris(2-  
535 carboxyethyl)phosphine (TCEP), 1 mM ATP, 2 mM magnesium sulphate, 15  $\mu$ g/ml  
536 cardiolipin, 50  $\mu$ g/ml 1-palmitoyl-2-oleoyl-sn-glycero-3-phosphocholine (POPC), 25  $\mu$ g/ml 1-  
537 palmitoyl-2-oleoyl-sn-glycero-3-phosphoethanolamine (POPE) and 10  $\mu$ g/ml 1-palmitoyl-2-  
538 oleoyl-sn-glycero-3-[phospho-rac-(1-glycerol)] (POPG). All phospholipids were purchased  
539 from Avanti Polar Lipids (catalog numbers 840012C, 850457C, 850757C and 840757,  
540 respectively). ATP synthase was eluted with a gradient of 20 mM reduced glutathione in Tris  
541 pH 8.0 buffer containing the same components as the binding buffer. Fractions containing ATP  
542 synthase were pooled and concentrated to 150  $\mu$ l on Vivaspin centrifugal concentrator with 30  
543 kDa molecular weight cut-off. The sample was fractionated by size exclusion chromatography  
544 on a Superose 6 Increase 3.2/300 GL column (Cytiva) equilibrated in a buffer containing 20  
545 mM Tris pH 8.0, 100 mM sodium chloride, 2 mM magnesium chloride, 0.1 % (w/v) GDN,  
546 3.75  $\mu$ g/ml cardiolipin, 12.5  $\mu$ g/ml POPC, 6.25  $\mu$ g/ml POPE and 2.5  $\mu$ g/ml POPG at 0.03  
547 ml/min. Fractions corresponding to ATP synthase were pooled, supplemented with 0.05%  
548 (w/v)  $\beta$ -DDM that we and others experimentally found to better preserve dimer assemblies in  
549 cryo-EM<sup>39</sup>, and concentrated to 50  $\mu$ l.

550

#### 551 Preparation of cryo-EM grids and data collection

552 Samples were vitrified on glow-discharged Quantifoil R1.2/1.3 Au 300-mesh grids after  
553 blotting for 3 sec, followed by plunging into liquid ethane using a Vitrobot Mark IV. 5,199  
554 movies were collected using EPU 1.9 on a Titan Krios (ThermoFisher Scientific) operated at  
555 300 kV at a nominal magnification of 165 kx (0.83 Å/pixel) with a Quantum K2 camera  
556 (Gatan) using a slit width of 20 eV. Data was collected with an exposure rate of 3.6  
557 electrons/px/s, a total exposure of 33 electrons/Å<sup>2</sup> and 20 frames per movie.

558

## 559 Image processing

560 Image processing was performed within the Scipion 2 framework<sup>40</sup>, using RELION-3.0 unless  
561 specified otherwise. Movies were motion-corrected using the RELION implementation of the  
562 MotionCor2. 294,054 particles were initially picked using reference-based picking in  
563 Gautomatch (<http://www.mrc-lmb.cam.ac.uk/kzhang/Gautomatch>) and Contrast-transfer  
564 function parameters were using GCTF<sup>41</sup>. Subsequent image processing was performed in  
565 RELION-3.0 and 2D and 3D classification was used to select 100,605 particles, which were  
566 then extracted in an unbinned 560-pixel box (Fig. S1). An initial model of the ATP synthase  
567 dimer was obtained using *de novo* 3D model generation. Using masked refinement with applied  
568 C<sub>2</sub> symmetry, a 2.7-Å structure of the membrane region was obtained following per-particle  
569 CTF refinement and Bayesian polishing. Following C<sub>2</sub>-symmetry expansion and signal  
570 subtraction of one monomer, a 3.7 Å map of the peripheral stalk was obtained. Using 3D  
571 classification (T=100) of aligned particles, with a mask on the F<sub>1</sub>/c-ring region, 10 different  
572 rotational substates were then separated and maps at 3.5-4.3 Å resolution were obtained using  
573 3D refinement. The authors note that the number of classes identified in this study likely  
574 reflects the limited number of particles, rather than the complete conformational space of the  
575 complex. By combining particles from all states belonging to main rotational state 1, a 3.7-Å  
576 map of the rotor and a 3.2-Å consensus map of the complete ATP synthase dimer with both  
577 rotors in main rotational state 1 were obtained.

578

## 579 Model building, refinement and data visualization

580 An initial atomic model of the static F<sub>o</sub> membrane region was built automatically using  
581 Buccaneer<sup>42</sup>. Subunits were subsequently assigned directly from the cryo-EM map, 15 of them  
582 corresponding to previously identified *T. brucei* ATP synthase subunits<sup>21</sup>, while three subunits  
583 (ATPTB14, ATPEG3, ATPEG4) were newly identified using BLAST searches. Manual model  
584 building was performed in Coot using the *T. brucei* F<sub>1</sub> (PDB 6F5D)<sup>13</sup> and homology models<sup>43</sup>  
585 of the *E. gracilis* OSCP and c-ring (PDB 6TDU)<sup>10</sup> as starting models. Ligands were manually  
586 fitted to the map and restraints were generated by the GRADE server  
587 (<http://grade.globalphasing.org>). Real-space refinement was performed in PHENIX using auto-  
588 sharpened, local-resolution-filtered maps of the membrane region, peripheral stalk tip,  
589 c-ring/central stalk and F<sub>1</sub>F<sub>o</sub> monomers in different rotational states, respectively, using  
590 secondary structure restraints. Model statistics were generated using MolProbity<sup>44</sup> and  
591 EMRinger<sup>44,5</sup> Finally, the respective refined models were combined into a composite ATP  
592 synthase dimer model and real-space refined against the local-resolution-filtered consensus  
593 ATP synthase dimer map with both monomers in rotational state 1, applying reference  
594 restraints. Figures of the structures were prepared using ChimeraX<sup>46</sup>, the proton half-channels  
595 were traced using HOLLOW<sup>47</sup>.

596

## 597 **Data availability**

598 The atomic coordinates have been deposited in the Protein Data Bank (PDB) and are available  
599 under the accession codes: XXXX (membrane-region), XXXX (peripheral stalk), XXXX  
600 (rotor), XXXX (F<sub>1</sub>F<sub>o</sub> dimer), XXXX (rotational state 1a), XXXX (rotational state 1b), XXXX

601 (rotational state 1c), XXXX (rotational state 1d), XXXX (rotational state 1e), XXXX  
602 (rotational state 2a), XXXX (rotational state 2b), XXXX (rotational state 2c), XXXX  
603 (rotational state 2d), XXXX (rotational state 3). The local resolution filtered cryo-EM maps,  
604 half maps, masks and FSC-curves have been deposited in the Electron Microscopy Data Bank  
605 with the accession codes: EMD-XXXX (membrane-region), EMD-XXXX (peripheral stalk),  
606 EMD-XXXX (rotor), EMD-XXXX (F<sub>1</sub>F<sub>o</sub> dimer), EMD-XXXX (rotational state 1a), EMD-  
607 XXXX (rotational state 1b), EMD-XXXX (rotational state 1c), EMD-XXXX (rotational state  
608 1d), EMD-XXXX (rotational state 1e), EMD-XXXX (rotational state 2a), EMD-XXXX  
609 (rotational state 2b), EMD-XXXX (rotational state 2c), EMD-XXXX (rotational state 2d),  
610 EMD-XXXX (rotational state 3).

611

## 612 **Acknowledgements**

613 We are grateful to Sir John E. Walker and Martin Montgomery for invaluable assistance with  
614 ATP synthase purification in the initial stage of the project. We acknowledge cryo-electron  
615 microscopy and tomography core facility of CIISB, Instruct-CZ Centre, supported by MEYS  
616 CR (LM2018127). This work was supported by the Czech Science Foundation grants number  
617 18-17529S to A.Z. and 20-04150Y to O.G. and by European Regional Development Fund  
618 (ERDF) and Ministry of Education, Youth and Sport (MEYS) project  
619 CZ.02.1.01/0.0/0.0/16\_019/0000759 to A.Z., Swedish Foundation for Strategic Research  
620 (FFL15:0325), Ragnar Söderberg Foundation (M44/16), European Research Council (ERC-  
621 2018-StG-805230), Knut and Alice Wallenberg Foundation (2018.0080), and EMBO Young  
622 Investigator Programme to A.A.

623

## 624 **Author contributions**

625 A.Z. and A.A. conceived and designed the work. O.G. prepared the sample for cryo-EM. O.G.  
626 and A.M. performed initial screening. A.M. processed the cryo-EM data and built the model.  
627 O.G., A.M. and A.A. analyzed the structure. B.P., C.H.Y., M.J., M.S., O.G. and A.Z. performed  
628 biochemical analysis. O.G., A.M., A.A. and A.Z. interpreted the data. O.G., A.M., A.A. and  
629 A.Z. wrote and revised the manuscript. All authors contributed to the analysis and approved  
630 the final version of the manuscript.

631

## 632 **Competing interests**

633 The authors declare no competing interests.

634

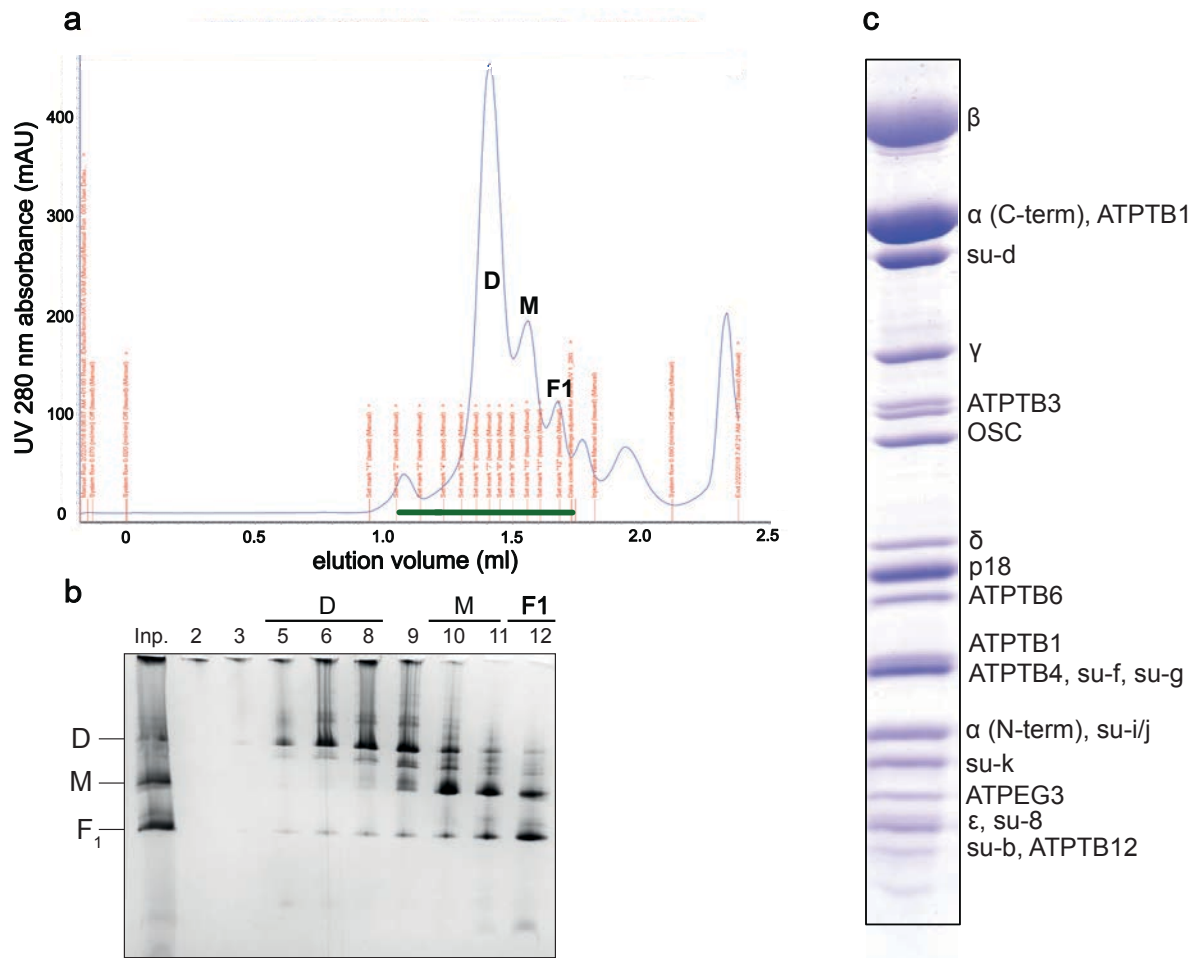
## 635 **References**

- 636 1. Paumard, P. et al. The ATP synthase is involved in generating mitochondrial cristae  
637 morphology. *EMBO J* **21**, 221-30 (2002).
- 638 2. Davies, K.M., Anselmi, C., Wittig, I., Faraldo-Gomez, J.D. & Kuhlbrandt, W. Structure  
639 of the yeast F<sub>1</sub>F<sub>o</sub>-ATP synthase dimer and its role in shaping the mitochondrial cristae.  
640 *Proc Natl Acad Sci U S A* **109**, 13602-7 (2012).

- 641 3. Panek, T., Elias, M., Vancova, M., Lukes, J. & Hashimi, H. Returning to the Fold for  
642 Lessons in Mitochondrial Crista Diversity and Evolution. *Curr Biol* **30**, R575-R588  
643 (2020).
- 644 4. Kuhlbrandt, W. Structure and Mechanisms of F-Type ATP Synthases. *Annu Rev*  
645 *Biochem* **88**, 515-549 (2019).
- 646 5. Spikes, T.E., Montgomery, M.G. & Walker, J.E. Structure of the dimeric ATP synthase  
647 from bovine mitochondria. *Proc Natl Acad Sci U S A* **117**, 23519-23526 (2020).
- 648 6. Pinke, G., Zhou, L. & Sazanov, L.A. Cryo-EM structure of the entire mammalian F-  
649 type ATP synthase. *Nat Struct Mol Biol* **27**, 1077-1085 (2020).
- 650 7. Guo, H., Bueler, S.A. & Rubinstein, J.L. Atomic model for the dimeric F<sub>o</sub> region of  
651 mitochondrial ATP synthase. *Science* **358**, 936-940 (2017).
- 652 8. Murphy, B.J. et al. Rotary substates of mitochondrial ATP synthase reveal the basis of  
653 flexible F<sub>1</sub>-F<sub>o</sub> coupling. *Science* **364**, eaaw9128 (2019).
- 654 9. Flygaard, R.K., Mühleip, A., Tobiasson, V. & Amunts, A. Type III ATP synthase is a  
655 symmetry-deviated dimer that induces membrane curvature through tetramerization.  
656 *Nature Communications* **11**, 5342 (2020).
- 657 10. Mühleip, A., McComas, S.E. & Amunts, A. Structure of a mitochondrial ATP synthase  
658 with bound native cardiolipin. *Elife* **8**, e51179 (2019).
- 659 11. Mühleip, A. et al. ATP synthase hexamer assemblies shape cristae of *Toxoplasma*  
660 mitochondria. *Nature Communications* **12**, 120 (2021).
- 661 12. Gahura, O. et al. The F<sub>1</sub>-ATPase from *Trypanosoma brucei* is elaborated by three  
662 copies of an additional p18-subunit. *FEBS J* **285**, 614-628 (2018).
- 663 13. Montgomery, M.G., Gahura, O., Leslie, A.G.W., Zikova, A. & Walker, J.E. ATP  
664 synthase from *Trypanosoma brucei* has an elaborated canonical F<sub>1</sub>-domain and  
665 conventional catalytic sites. *Proc Natl Acad Sci U S A* **115**, 2102-2107 (2018).
- 666 14. Serricchio, M. et al. Depletion of cardiolipin induces major changes in energy  
667 metabolism in *Trypanosoma brucei* bloodstream forms. *FASEB J* **35**, 21176 (2020).
- 668 15. Mühleip, A.W., Dewar, C.E., Schnauffer, A., Kuhlbrandt, W. & Davies, K.M. In situ  
669 structure of trypanosomal ATP synthase dimer reveals a unique arrangement of  
670 catalytic subunits. *Proc Natl Acad Sci U S A* **114**, 992-997 (2017).
- 671 16. Schnauffer, A., Clark-Walker, G.D., Steinberg, A.G. & Stuart, K. The F<sub>1</sub>-ATP synthase  
672 complex in bloodstream stage trypanosomes has an unusual and essential function.  
673 *EMBO J* **24**, 4029-40 (2005).
- 674 17. Brown, S.V., Hosking, P., Li, J. & Williams, N. ATP synthase is responsible for  
675 maintaining mitochondrial membrane potential in bloodstream form *Trypanosoma*  
676 *brucei*. *Eukaryot Cell* **5**, 45-53 (2006).
- 677 18. Gahura, O., Hierro-Yap, C. & Zikova, A. Redesigned and reversed: Architectural and  
678 functional oddities of the trypanosomal ATP synthase. *Parasitology* **148**, 1151-1160  
679 (2021).
- 680 19. Hierro-Yap, C. et al. Bioenergetic consequences of F<sub>o</sub>F<sub>1</sub>-ATP synthase/ATPase  
681 deficiency in two life cycle stages of *Trypanosoma brucei*. *J Biol Chem* **296**, 100357  
682 (2021).

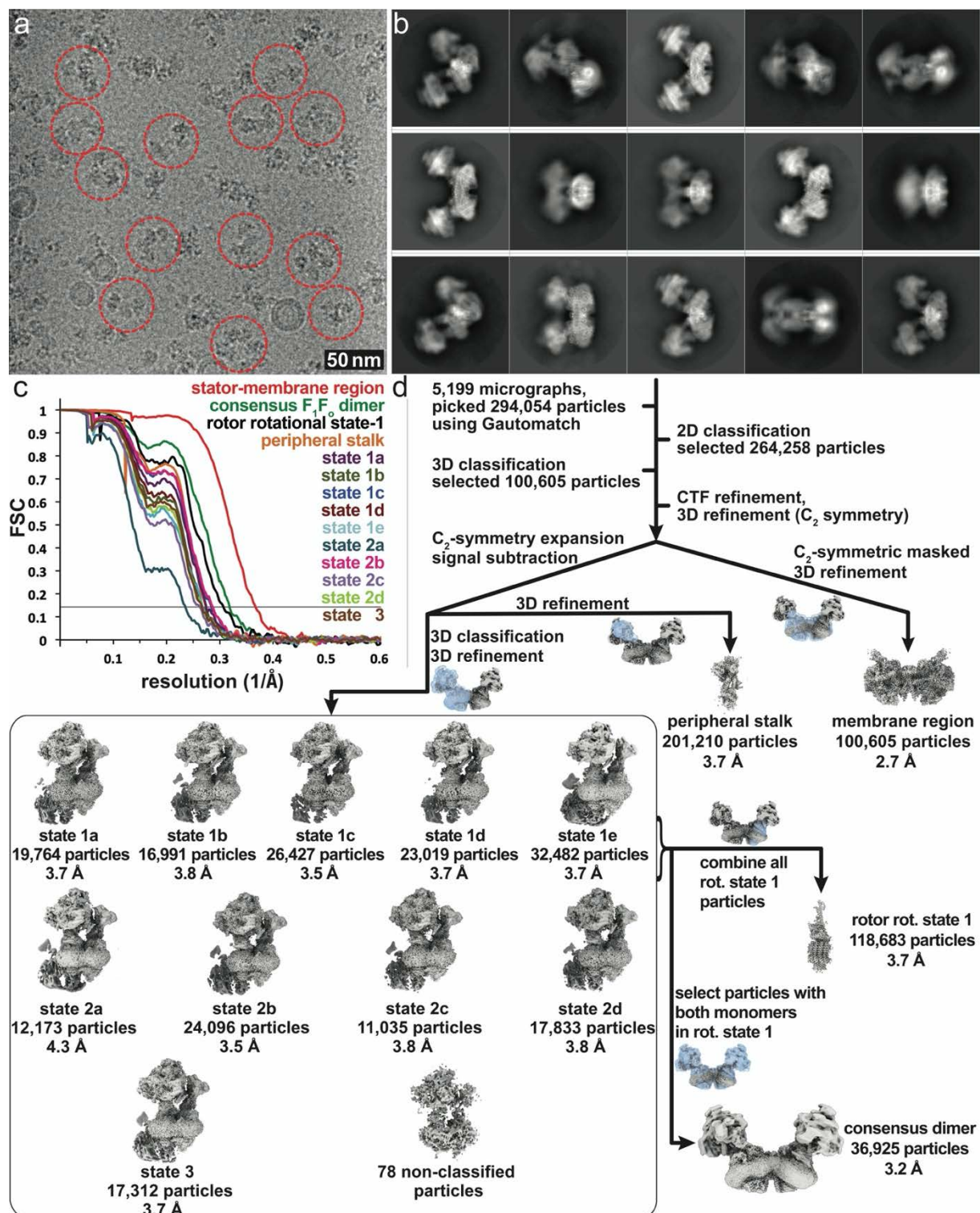
- 683 20. Gahura, O., Panicucci, B., Vachova, H., Walker, J.E. & Zikova, A. Inhibition of F<sub>1</sub>-  
684 ATPase from *Trypanosoma brucei* by its regulatory protein inhibitor TbIF1. *FEBS J*  
685 **285**, 4413-4423 (2018).
- 686 21. Zikova, A., Schnauffer, A., Dalley, R.A., Panigrahi, A.K. & Stuart, K.D. The F(0)F(1)-  
687 ATP synthase complex contains novel subunits and is essential for procyclic  
688 *Trypanosoma brucei*. *PLoS Pathog* **5**, e1000436 (2009).
- 689 22. Perez, E. et al. The mitochondrial respiratory chain of the secondary green alga *Euglena*  
690 *gracilis* shares many additional subunits with parasitic Trypanosomatidae.  
691 *Mitochondrion* **19 Pt B**, 338-49 (2014).
- 692 23. Sathish Yadav, K.N. et al. Atypical composition and structure of the mitochondrial  
693 dimeric ATP synthase from *Euglena gracilis*. *Biochim Biophys Acta* **1858**, 267-275  
694 (2017).
- 695 24. Dewar, C.E., Oeljeklaus, S., Warscheid, B. and Schneider, A. Characterisation of a  
696 highly diverged mitochondrial ATP synthase peripheral stalk subunit b in *Trypanosoma*  
697 *brucei* (2021).  
698 <https://www.biorxiv.org/content/10.1101/2021.10.13.464200v1>
- 699 25. Aphasizheva, I. et al. Lexis and Grammar of Mitochondrial RNA Processing in  
700 Trypanosomes. *Trends Parasitol* **36**, 337-355 (2020).
- 701 26. Blum, B., Bakalara, N. & Simpson, L. A model for RNA editing in kinetoplastid  
702 mitochondria: "guide" RNA molecules transcribed from maxicircle DNA provide the  
703 edited information. *Cell* **60**, 189-98 (1990).
- 704 27. Adler, B.K., Harris, M.E., Bertrand, K.I. & Hajduk, S.L. Modification of *Trypanosoma*  
705 *brucei* mitochondrial rRNA by posttranscriptional 3' polyuridine tail formation. *Mol*  
706 *Cell Biol* **11**, 5878-84 (1991).
- 707 28. Hofer, A., Steverding, D., Chabes, A., Brun, R. & Thelander, L. *Trypanosoma brucei*  
708 CTP synthetase: a target for the treatment of African sleeping sickness. *Proc Natl Acad*  
709 *Sci U S A* **98**, 6412-6 (2001).
- 710 29. Gupta, K. et al. The role of interfacial lipids in stabilizing membrane protein oligomers.  
711 *Nature* **541**, 421-424 (2017).
- 712 30. Arnold, I., Pfeiffer, K., Neupert, W., Stuart, R.A. & Schagger, H. Yeast mitochondrial  
713 F<sub>1</sub>F<sub>0</sub>-ATP synthase exists as a dimer: identification of three dimer-specific subunits.  
714 *EMBO J* **17**, 7170-8 (1998).
- 715 31. Gu, J. et al. Cryo-EM structure of the mammalian ATP synthase tetramer bound with  
716 inhibitory protein IF1. *Science* **364**, 1068-1075 (2019).
- 717 32. Spikes, T.E., Montgomery, M.G. & Walker, J.E. Interface mobility between monomers  
718 in dimeric bovine ATP synthase participates in the ultrastructure of inner mitochondrial  
719 membranes. *Proc Natl Acad Sci U S A* **118**, e2021012118 (2021).
- 720 33. Cadena, L.R. et al. Mitochondrial contact site and cristae organization system and F<sub>1</sub>F<sub>0</sub>-  
721 ATP synthase crosstalk is a fundamental property of mitochondrial cristae. *mSphere* **6**,  
722 e0032721 (2021).
- 723 34. Davies, K.M. et al. Macromolecular organization of ATP synthase and complex I in  
724 whole mitochondria. *Proc Natl Acad Sci U S A* **108**, 14121-6 (2011).

- 725 35. Blum, T.B., Hahn, A., Meier, T., Davies, K.M. & Kühlbrandt, W. Dimers of  
726 mitochondrial ATP synthase induce membrane curvature and self-assemble into rows.  
727 *Proc Natl Acad Sci U S A* **116**, 4250-4255 (2019).
- 728 36. Bochud-Allemann, N. & Schneider, A. Mitochondrial substrate level phosphorylation  
729 is essential for growth of procyclic *Trypanosoma brucei*. *J Biol Chem* **277**, 32849-54  
730 (2002).
- 731 37. Poon, S.K., Peacock, L., Gibson, W., Gull, K. & Kelly, S. A modular and optimized  
732 single marker system for generating *Trypanosoma brucei* cell lines expressing T7 RNA  
733 polymerase and the tetracycline repressor. *Open Biol* **2**, 110037 (2012).
- 734 38. Allemann, N. & Schneider, A. ATP production in isolated mitochondria of procyclic  
735 *Trypanosoma brucei*. *Mol Biochem Parasitol* **111**, 87-94 (2000).
- 736 39. Aibara, S., Dienemann, C., & Cramer, P.. Structure of an inactive RNA polymerase II  
737 dimer. *Nucleic Acids Research*, gkab783 (2021).
- 738 40. de la Rosa-Trevin, J.M. et al. Scipion: A software framework toward integration,  
739 reproducibility and validation in 3D electron microscopy. *J Struct Biol* **195**, 93-9  
740 (2016).
- 741 41. Zhang, K. Gctf: Real-time CTF determination and correction. *J Struct Biol* **193**, 1-12  
742 (2016).
- 743 42. Cowtan, K. The Buccaneer software for automated model building. 1. Tracing protein  
744 chains. *Acta Crystallogr D Biol Crystallogr* **62**, 1002-11 (2006).
- 745 43. Waterhouse, A. et al. SWISS-MODEL: homology modelling of protein structures and  
746 complexes. *Nucleic Acids Res* **46**, W296-W303 (2018).
- 747 44. Williams, C.J., Headd, J.J., Moriarty, N.W., Prisant, M.G., Videau, L.L., Deis, L.N.,  
748 Verma, V., Keedy, D.A., Hintze, B.J., Chen, V.B. and Jain, S. MolProbity: More and  
749 better reference data for improved all-atom structure validation. *Protein Science*, **27**,  
750 293-315 (2018).
- 751 45. Barad, B.A., Echols, N., Wang, R.Y.R., Cheng, Y., DiMaio, F., Adams, P.D. and Fraser,  
752 J.S. EMRinger: side chain-directed model and map validation for 3D cryo-electron  
753 microscopy. *Nature methods*, **12**, 943-946 (2015).
- 754 46. Goddard, T.D. et al. UCSF ChimeraX: Meeting modern challenges in visualization and  
755 analysis. *Protein Sci* **27**, 14-25 (2018).
- 756 47. Ho, B.K. & Gruswitz, F. HOLLOW: generating accurate representations of channel  
757 and interior surfaces in molecular structures. *BMC Struct Biol* **8**, 49 (2008).

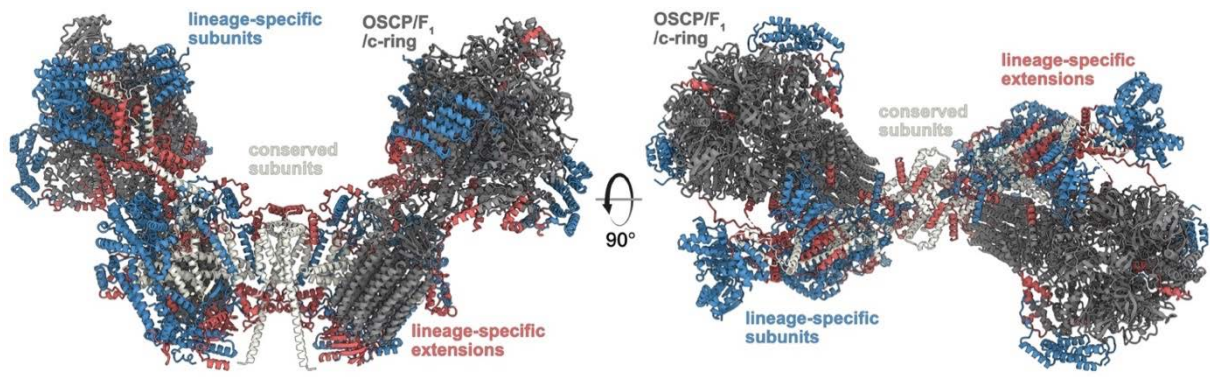


**Extended Data Fig. 1 Purification of the *T. brucei* ATP synthase dimer.**

**a**, Size exclusion chromatography trace with peaks enriched with ATP synthase dimers (D), monomers (M) and F<sub>1</sub>-ATPase (F<sub>1</sub>) labelled. **b**, Fractions from size exclusion chromatography marked with green bar in (a) resolved by native BN-PAGE. **c**, Dimer-enriched fraction resolved by SDS-PAGE stained by Coomassie blue dye. Bands are annotated based on mass spectrometry identification from excised gel pieces.

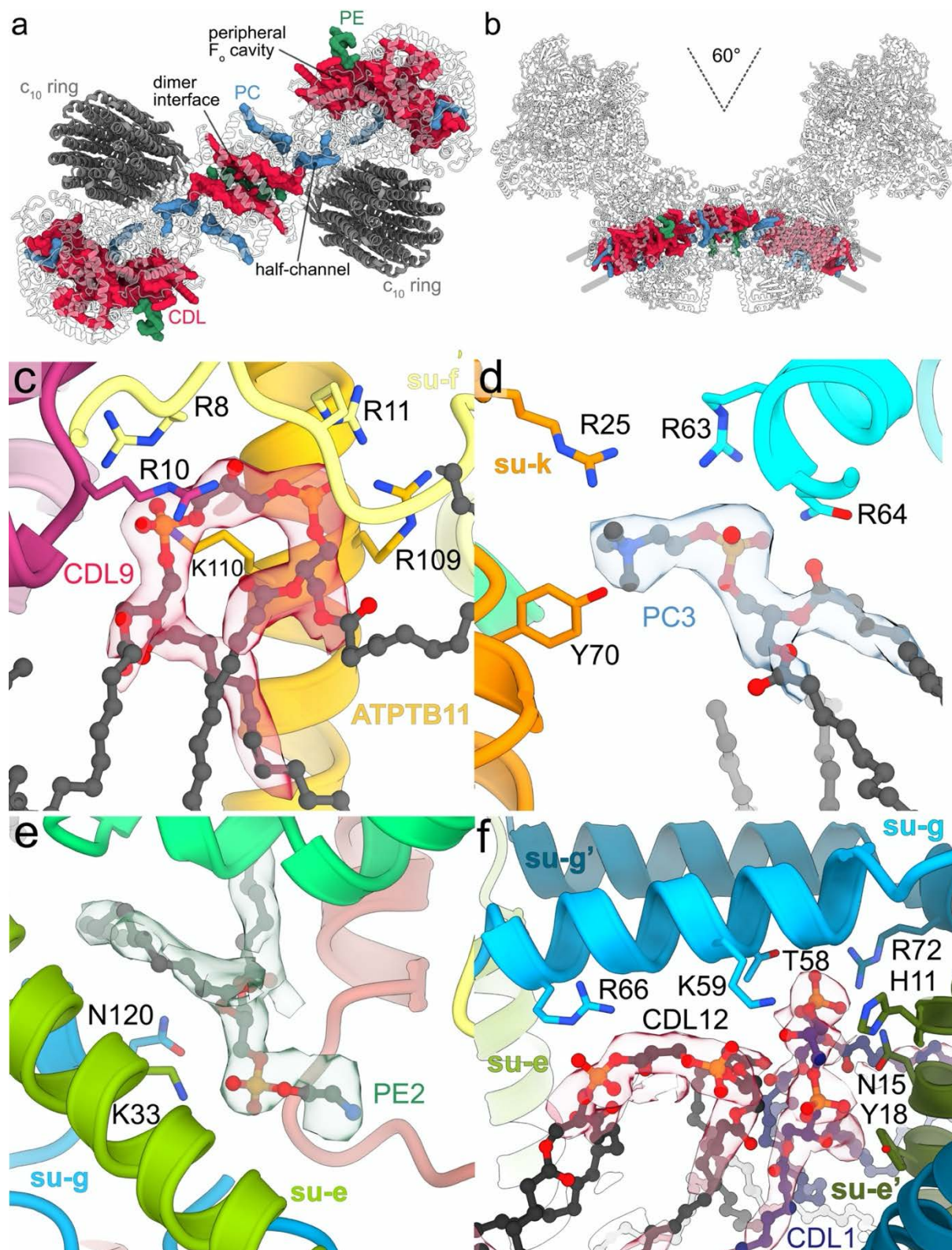


**Extended Data Fig. 2 Cryo-EM data processing of the *T. brucei* ATP synthase dimer.** **a**, Representative micrograph. **b**, 2D class averages. **c**, Fourier Shell Correlation (FSC) curves showing the estimated resolutions of ATP synthase maps according to the gold standard 0.143 criterion. **d**, Data processing scheme resulting in maps covering all regions of the complex, as well as 10 rotational states.



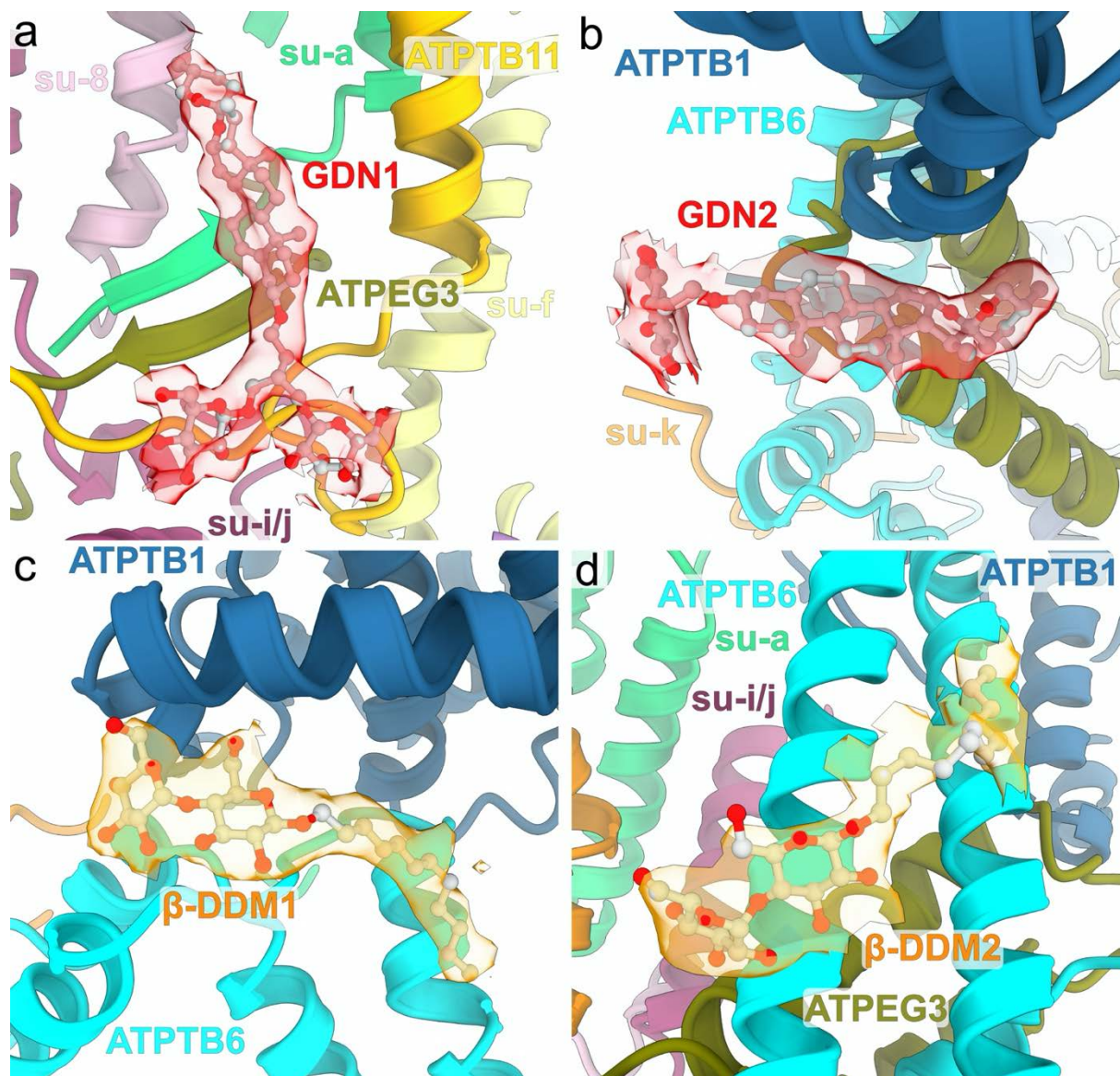
**Extended Data Fig. 3 Conserved and phylum specific elements generate the *T. brucei* ATP synthase architecture.**

The canonical OSCP/F<sub>1</sub>/c-ring monomers (dark grey) are tied together by both conserved F<sub>o</sub> subunits and extensions of lineage-specific subunits (red). The F<sub>o</sub> periphery and peripheral stalk attachment are composed of lineage specific subunits (blue).



**Extended Data Fig. 4 The F<sub>0</sub> region coordinates numerous bound lipids.**

**a**, F<sub>0</sub> top view, cardiolipin (CDL), phosphatidylcholine (PC) and phosphatidylethanolamine (PE) are bound at the dimer interface, the luminal proton half-channel and the peripheral F<sub>0</sub> cavity. **b**, The 60°-dimer angle generates a curved F<sub>0</sub> region with phospholipids bound in an arc-shaped bilayer. **c-f**, Bound lipids with cryo-EM density and coordinating residues.



**Extended Data Fig. 5 Bound detergents of the F<sub>0</sub> region.**

GDN (a,b) and  $\beta$ -DDM (c,d) molecules bound in the periphery of the membrane region with cryo-EM map densities shown (transparent), indicating that both glycosides are retained in the detergent micelle.

```

PDB_6TDV_su-b_E.gracilis  DKDVPMSILHETHGLSYVNWCM SLAPGLLVFEGFFRARYYRSRVPPSRTVL
tr|Q580A0|Q580A0_TRYB2    RRLVPRVMMAPMGGA-TALCTSRGYNMLVFRDPK-----RRPQL
                          : **  :: . * : . * * . .:***..          * . *

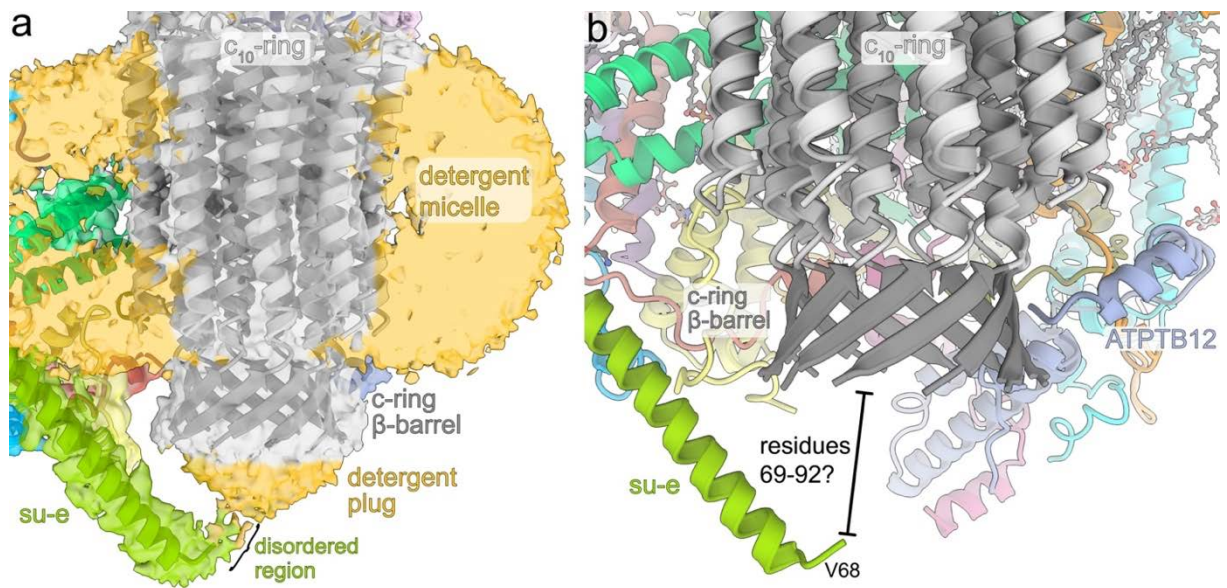
PDB_6TDV_su-b_E.gracilis  MNGLKMRMFSLARQQAPKIVHK-----PVLSPPIPEHLRLVKNVA
tr|Q580A0|Q580A0_TRYB2    SDEE-----RAKVVVNQAEWP EEFKDFDPDDPYKNSPEI IKGMS
                          :                .*: * :                .* : .:***::

PDB_6TDV_su-b_E.gracilis  QVQIDMLKLLNAQAAK
tr|Q580A0|Q580A0_TRYB2    SWNLFLWGVECAFIYQ
                          . :: : : * :

```

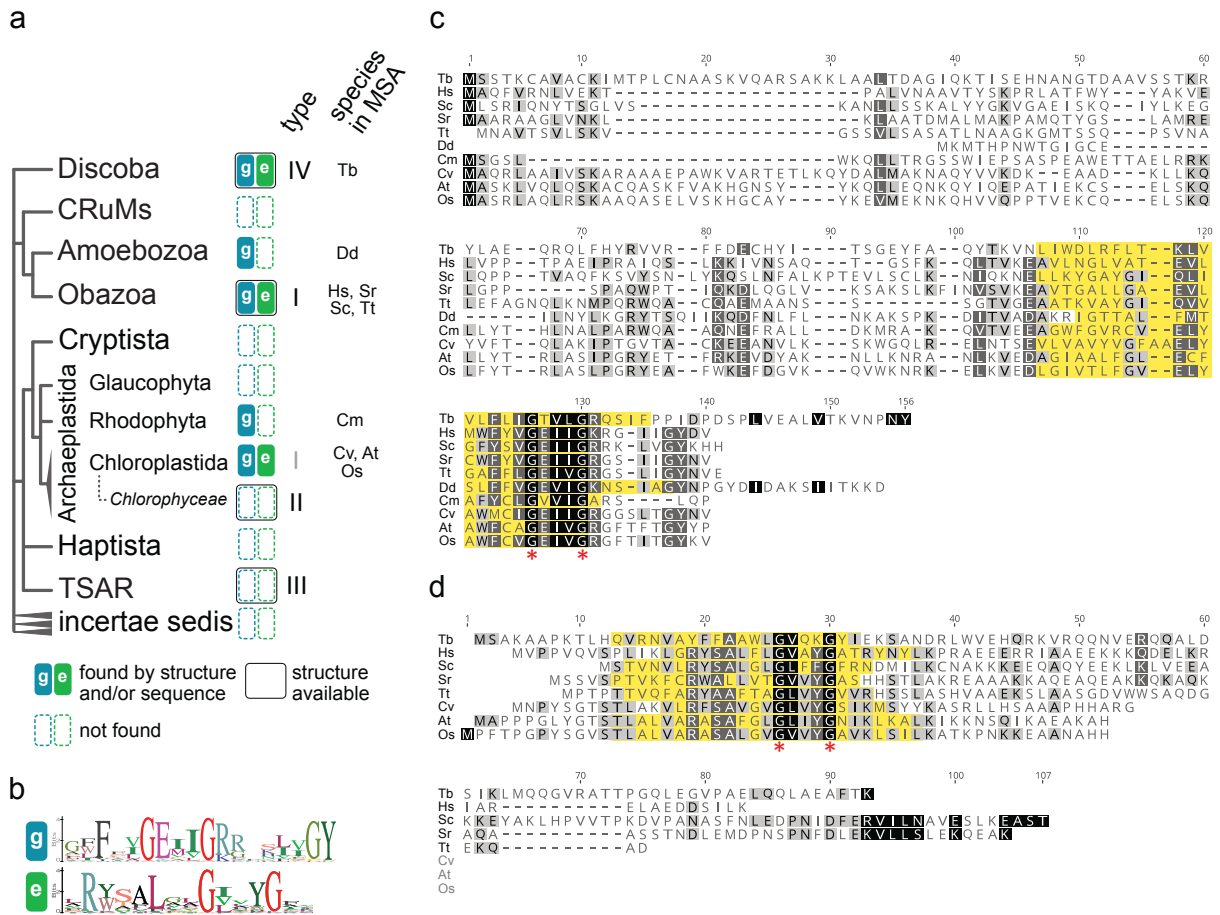
**Extended Data Fig. 6 Sequence alignment of subunit-*b* with *E. gracilis*.**

The *E. gracilis* sequence was retrieved from the PDB ID 6TDV<sup>1</sup> and aligned with the current work using ClustalW<sup>2</sup>. Both sequences represent reduced versions of subunit-*b* that are structurally conserved and occupy similar positions in the models. Termini were removed.



**Extended Data Fig. 7 The C-terminal tail of subunit-*e* interacts with the  $c_{10}$ -ring.**

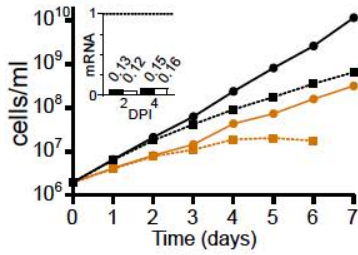
**a**, The cryo-EM map reveals disordered detergent density of the detergent belt surrounding the membrane region as well as a detergent plug on the luminal side of the  $c$ -ring. **b**, The helical C-terminus of subunit-*e* extends into the lumen towards the  $c$ -ring. The terminal 23 residues are disordered and likely interact with the  $\beta$ -barrel.



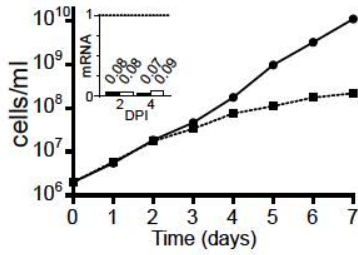
## Extended Data Fig. 8 Phylogenetic distribution and sequence conservancy of subunit-*e* and -*g*.

**a**, Distribution of subunits *e* and *g* mapped on the phylogenetic tree of eukaryotes<sup>3</sup>. Homologs of subunits *e* and *g* were searched in non-redundant GenBank and UniprotKB protein databases by PSI-BLAST, and phmmer and hmmsearch<sup>4</sup>, respectively, using individual sequences of representatives from *H. sapiens* and *T. brucei*, and in the case of hmmsearch a multiple sequence alignment (MSA) of representatives from *Homo sapiens*, *Saccharomyces cerevisiae*, *Arabidopsis thaliana* and *T. brucei*, as queries. Groups, in which at least one structure of ATP synthase is available, are marked. Abbreviations of species used in MSA in panels (c) and (d) are shown. **b**, Sequence logo of GXXXG motifs and flanking regions of subunits *e* and *g*. Hits from hmmsearch were clustered by CD-HIT Suite<sup>5</sup> to 50% sequence identity and MSA of representative sequences of each cluster was generated by Clustal Omega<sup>6</sup>. The sequence logos were created from MSA in Geneious Prime (Biomatters Ltd.). **c,d**, MSA of sequences of subunits *g* (c) and *e* (d) from species representing major groups shown in (a) generated by MUSCLE<sup>7</sup> and visualized in Geneious Prime. The experimentally determined or predicted transmembrane regions are highlighted in yellow. Species abbreviations: Tb – *T. brucei*, Hs – *H. sapiens*, Sc – *S. cerevisiae*, Sr – *Salpingoeca rosetta*, Tt – *Thecamonas trahens*, Dd – *Dictyostelium discoideum*, Cm – *Cyanidioschyzon merolae*, Cv – *Chlorella vulgaris*, At – *Arabidopsis thaliana*, Os – *Oryza sativa*.

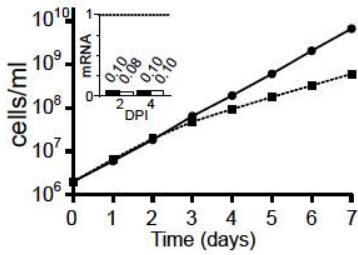
**a**  
**su-e RNAi**



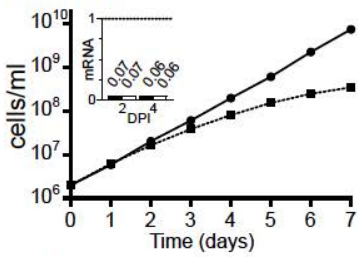
**su-f RNAi**



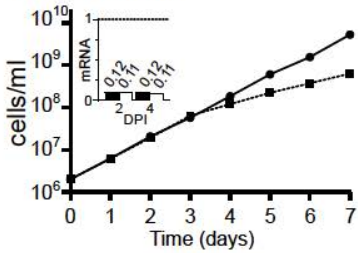
**su-i/j RNAi**



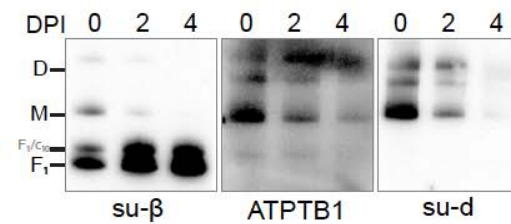
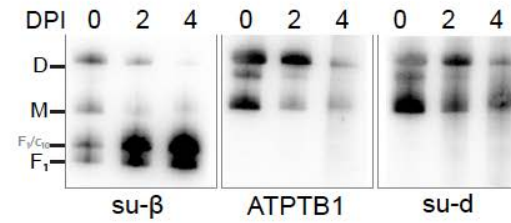
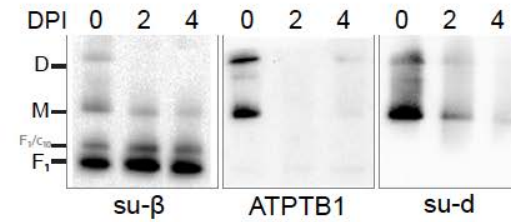
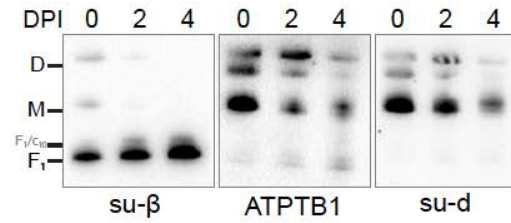
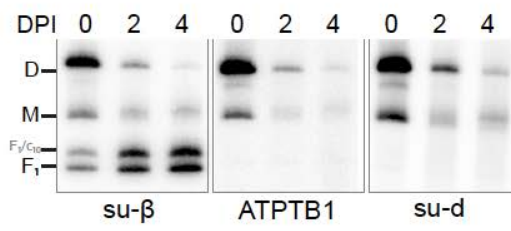
**su-k RNAi**



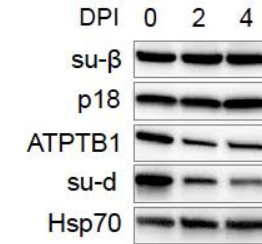
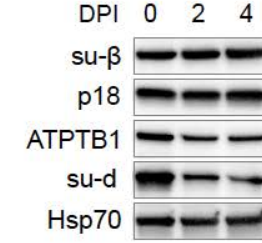
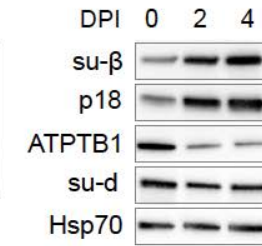
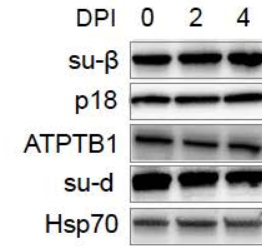
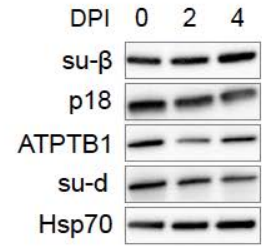
**ATPTB3 RNAi**

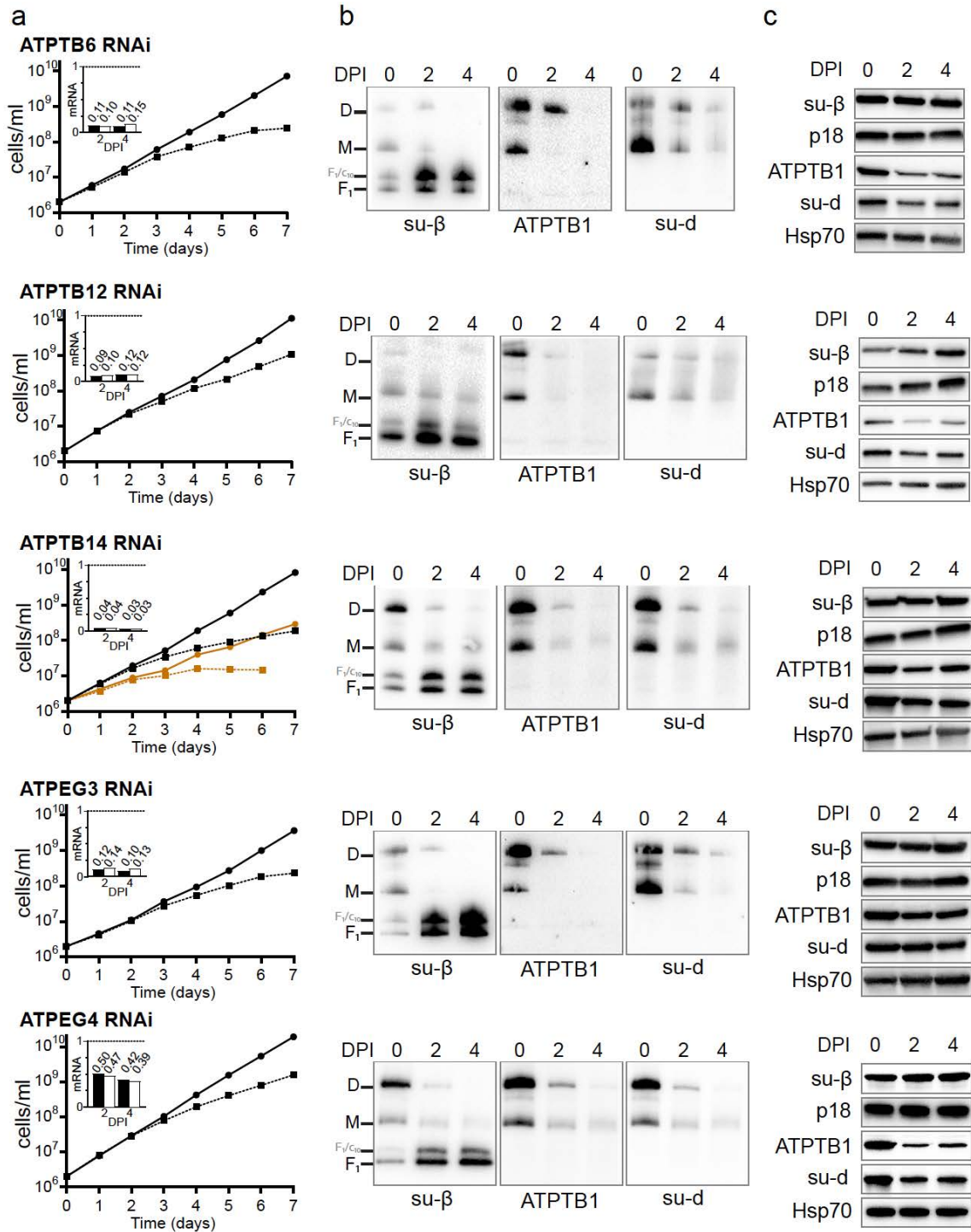


**b**



**c**





**Extended Data Fig. 9 Effects of RNAi knock-down of ATP synthase subunits on viability and stability and dimerization of ATP synthase.**

**a**, Growth curves of indicated non-induced (solid lines) and tetracycline induced (dashed lines) RNAi cell lines in the presence (black) or absence (brown) of glucose. The insets show relative levels of the respective target mRNA at indicated days post induction (DPI) normalized to the levels of 18S rRNA (black bars) or  $\beta$ -tubulin (white bars). **b**, Immunoblots of mitochondrial lysates from indicated RNAi cell lines resolved by BN-PAGE probed by antibodies against indicated ATP synthase subunits. **c**, Immunoblots of whole cell lysates from indicated RNAi cell lines probed with indicated antibodies.

	Membrane region	Rotor	Peripheral stalk	F <sub>1</sub> F <sub>0</sub> dimer	Rot. 1a	Rot. 1b	Rot. 1c	Rot. 1d	Rot. 1e	Rot. 2a	Rot. 2b	Rot. 2c	Rot. 2d	Rot. 3
<b>Data collection</b>														
Microscope	Titan Krios													
Voltage (kV)	300													
Camera	K2 Summit													
Magnification	165 kx													
Exposure (e <sup>-</sup> /Å <sup>2</sup> )	33													
Defocus range (µm)	-1.6 to -3.2													
Pixel size (Å)	0.83													
Movies collected	5,199													
Frames per movie	20													
<b>Data processing</b>														
Initial particles	100,605 (C <sub>2</sub> symmetry-expanded: 201,210)													
Final no. particles	100,605	118,683	201,210	36,925	19,764	26,427	23,019	16,991	34,482	12,173	24,096	11,035	17,833	17,312
Symmetry	C <sub>2</sub>	C <sub>1</sub>	C <sub>1</sub>	C <sub>2</sub>	C <sub>1</sub>									
Map resolution (Å)	2.7	3.7	3.7	3.2	3.7	3.5	3.7	3.8	3.7	4.3	3.5	3.8	3.8	3.7
Sharpening B factor	-46.2	-74.4	-92.5	-49.8	-61.8	-61.1	-57.6	-45.6	-58.0	-73.8	-54.5	-65.2	-54.9	-61.7
<b>EMD ID</b>														
<b>Model refinement statistics</b>														
CC (map/model)	0.86	0.83	0.82	0.71	0.79	0.79	0.82	0.79	0.69	0.71	0.81	0.77	0.77	0.79
Resolution (map/model)	2.65	3.4	3.68	3.13	3.48	3.56	3.36	3.55	3.57	3.94	3.39	3.73	3.64	3.58
No. of atoms	76,690	19,669	12,083	251,552	129,568	129,568	129,568	129,568	129,568	129,563	129,563	129,563	129,563	129,566
No. of residues	4074	1285	767	15,356	7872	7872	7872	7872	7872	7872	7872	7872	7872	7872
No. of lipids	36	0	0	36	21	21	21	21	21	21	21	21	21	21
No. of ATP/ADP	0	0	0	10	5	5	5	5	5	5	5	5	5	5
No. of Mg ions	0	0	0	10	5	5	5	5	5	5	5	5	5	5
<b>B-factor (Å<sup>2</sup>)</b>														
- protein	54.05	56.13	77.88	84.48	55.65	70.37	80.22	83.27	70.70	112.72	79.93	65.52	66.49	101.5
- ligands	50.57	58.25	-	69.94	40.99	72.29	63.18	78.43	63.76	75.25	74.47	61.79	46.55	83.68
Rotamer outliers (%)	0.44	0.40	0.31	0.22	0.42	0.09	0.18	0.26	0.58	0.18	0.27	0.48	0.42	0.39
<b>Ramachandran (%)</b>														
- outliers	0.00	0.00	0.00	0.01	0.001	0.003	0.004	0.01	0.003	0.01	0.00	0.04	0.04	0.04
- allowed	1.57	1.91	1.59	1.56	1.52	1.65	1.44	1.49	1.49	1.67	1.58	1.47	1.65	1.79
- favored	98.43	98.08	98.41	98.42	98.47	98.34	98.56	98.49	98.48	98.31	98.42	98.49	98.31	98.17
Clash score	1.66	2.44	2.32	2.26	2.60	2.65	2.53	2.67	2.99	2.38	2.30	2.52	2.38	3.57
MolProbity score	0.92	1.03	1.01	1.00	1.05	1.05	1.04	1.05	1.09	1.02	1.01	1.04	1.02	1.15
<b>RMSD</b>														
- bonds (Å)	0.004	0.004	0.02	0.003	0.003	0.003	0.004	0.003	0.003	0.002	0.003	0.003	0.003	0.003
- angles (°)	0.455	0.416	0.386	0.407	0.414	0.424	0.417	0.407	0.412	0.410	0.416	0.419	0.428	0.421
EMRinger score	5.11	3.96	1.61	2.56	3.24	2.95	3.32	2.85	3.32	1.35	2.89	2.32	2.49	2.8
<b>PDB ID</b>														

**Extended Data Table 1. Data collection, processing, model refinement and validation statistics.**

Subunit name	TriTrypDB Lister strain 427 ID	TriTrypDB TREU927 strain ID	Uniprot TREU927 strain ID	Residues	Residues built
<b>F<sub>1</sub> subcomplex</b>					
$\alpha$	Tb427_070081800 Tb427_070081900	Tb927.7.7420 Tb927.7.7430	Q57TX9	584	45-151, 161-584
$\beta$	Tb427_030013500	Tb927.3.1380	Q57XX1	519	26-514
$\gamma$	Tb427_100005200	Tb927.10.180	B0Z0F6	305	2-301
$\delta$	Tb427_060054900	Tb927.6.4990	Q586H1	182	22-182
$\epsilon$	Tb427_100054600	Tb427.10.5050	N/A	75	11-75
<b>p18</b>	Tb427_050022900	Tb927.5.1710	Q57ZP0	188	23-188
<b>F<sub>0</sub> subcomplex</b>					
<b>OSCP</b>	Tb427_100087100	Tb927.10.8030	Q38AG1	255	18-202, 208-255
<b>a</b>	mt encoded	mt encoded	N/A	231	1-231
<b>b</b>	Tb427_040009100	Tb927.4.720	Q580A0	105	26-105
<b>c</b>	Tb427_100018700 Tb427_110057900 Tb427_070019000	Tb927.10.1570 Tb927.11.5280 Tb927.7.1470	Q38C84 Q385P0 Q57WQ3	118	41-118
<b>d</b>	Tb427_050035800	Tb927.5.2930	Q57ZW9	370	17-325, 332-354
<b>e</b>	Tb427_110010200	Tb927.11.600	N/A	92	1-383
<b>f</b>	Tb427_030016600	Tb927.3.1690	Q57ZE2	145	2-136
<b>g</b>	Tb427_020016900	Tb927.2.3610	Q586X8	144	16-144
<b>i/j</b>	Tb427_030029400	Tb927.3.2880	Q57ZM4	104	2-104
<b>k</b>	Tb427_070011800	Tb927.7.840	Q57VT0	124	20-124
<b>8</b>	Tb427_040037300	Tb927.4.3450	Q585K5	114	29-114
<b>ATBTB1</b>	Tb427_100008400	Tb927.10.520	Q38CI8	396	1-383
<b>ATPTB3</b>	Tb427_110067400	Tb927.11.6250	Q385E4	269	2-269
<b>ATPTB4</b>	Tb427_100105100	Tb927.10.9830	Q389Z3	157	21-157
<b>ATPTB6</b>	Tb427_110017200	Tb927.11.1270	Q387C5	169	2-169
<b>ATPTB11</b>	Tb427_030021500	Tb927.3.2180	Q582T1	156	18-156
<b>ATPTB12</b>	Tb427_050037400	Tb927.5.3090	Q57Z84	101	5-100
<b>ATPEG3</b>	Tb427_060009300	Tb927.6.590	Q583U4	98	14-98
<b>ATPEG4</b>	N/A	Tb927.11.2245	N/A	62	1-62

**Extended Data Table 2. Composition of *T. brucei* ATP synthase dimer.**

Subunit	Primer pair sequences
<b>Primers for amplification of RNAi cassettes</b>	
<i>b</i>	TAATCTCGAGGGTACCGTTGAGTGAGGAGGAACGGG GCAGTCTAGAGGATCCTATCCCTTCCACCCACCACT
<i>e</i>	TAATCTCGAGGGTACCGGGAGTACAGAAGGGCTACA TAGATCTAGAGGATCCCGTGCACACCATCAGCTG
<i>f</i>	ATACTCGAGGGTACCGTGAGTACCGCCTTTACGC GCGTCTAGAGGATCCAGCACTGATCACCAAACCTGC
<i>g</i>	ACTGCTCGAGGGTACCACGCGGGAATTCAAAAGACC GCGGTCTAGAGGATCCCGTTGCGGTGCTTGTCATTA
<i>ij</i>	TAATCTCGAGGGTACCGAATATCCGATGCATGCCGC GCCGTCTAGAGGATCCACTTCGCTCTACTGCATGCA
<i>k</i>	ATTACTCGAGCCC GGGCGATCAGTGCAGGGGATTTT GCCGTCTAGAGGATCCTTTCCTCGAAAACGCACACA
<b>8</b>	ATGACTCGAGGGTACCGGGCTATGGTGTGGTATTATGC GACGTCTAGAGGATCCGCAGAAAACCTCCAACGACA
<b>ATPTB3</b>	ACTGCTCGAGGGTACCAAAGAGGAGGTGAGGTCTGC GCAGTCTAGAGGATCCCCCTAGGGTTCTTCGAAGCA
<b>ATPTB4</b>	CTGACTCGAGGGTACCTTCCTTTTCTGCTGCATCGG GCAGTCTAGAGGATCCCTCCTCGGGCTTCCAATTTG
<b>ATPTB6</b>	ACTGCTCGAGGGTACCCAACATGGCAGTATCCGGTG GCAGTCTAGAGGATCCTTATTAGTGGCGGTGGTGGT
<b>ATPTB11</b>	ACTGCTCGAGGGTACCGCGCTCGTCTTCTCCATTTT GCAGAAGCTTGGATCCAGGTTGGGGTGTTTAGGGAG
<b>ATPTB12</b>	TAATCTCGAGGGTACCGACGCCATCAAAGGAATGCC GCCGTCTAGAGGATCCAGCAGCCAACAAACAGACAA
<b>ATPEG3</b>	TACACTCGAGGGTACCAAACCTGAAGGCCCTCACAC GCAGTCTAGAGGATCCCTCTTTCTGTCGCGCCTGATA
<b>Primers for quantification of mRNA levels by qPCR</b>	
<i>b</i>	CCAAGAGTGATGATGGCCCC CGTTTAGGGTCGCGGAAAAC
<i>e</i>	CAAGCCTTGCACACACTTTATG CCGCAAAGAAGTACGCCAC
<i>f</i>	TTTTCTACATACCGCAGCAGT TACCATTCCATGCGCGTTG
<i>g</i>	GCAATTGTGTGAGCTGAACG TACTGGCCGCATTGCATAAC
<i>ij</i>	AGAGTAAAAGCGCGCCTACG

	CAGTTGGAAAACCGGTAGCC
<i>k</i>	ACACAAAACACTTCCAGCAGA CGCTATGACGGACAGGTGT
<b>8</b>	GCTACGGCGACTTGGTGC CGTCACCGCGTATTGTTCA
<b>ATPTB3</b>	AACGTTTATATCAGCGGGCG CTGTTTTGGTCTGCACACGA
<b>ATPTB4</b>	CCAAACTTTGAAGCAGCGGA ATTCTTGGATCCGCACCTT
<b>ATPTB6</b>	TCGGCATAGGAGAAGTAACGA GATTCGGTTTGGA ACTTGCG
<b>ATPTB11</b>	CAACGGCCCCACATTCTC ACACCGCGGTCATTCATTG
<b>ATPTB12</b>	GCACTTCATTCTCCCGACTG ACATGATGTAACACCTCCGC
<b>ATPEG3</b>	TGGCCCCACATGACTGAAAA GGAAGTGATCCGCCGGATT

**Extended Data Table 3. List of primers used in the study.**

<b>Target</b>	<b>Type</b>	<b>Reference</b>	<b>Dilution SDS-PAGE</b>	<b>Dilution BN-PAGE</b>
<b>Primary antibodies</b>				
<b>subunit-<math>\beta</math></b>	rabbit polyclonal	1	1:2000	1:2000
<b>p18</b>	rabbit polyclonal	1	1:1000	-
<b>ATPTB1</b>	rabbit polyclonal	1	1:1000	1:1000
<b>subunit-<i>d</i></b>	rabbit polyclonal	1	1:1000	1:500
<b>mtHsp70</b>	mouse monoclonal	2	1:5000	-
<b>Secondary antibodies</b>				
<b>goat anti-rabbit IgG HRP conjugate</b>		BioRad 1721019	1:2000	1:2000
<b>goat anti-mouse IgG HRP conjugate</b>		BioRad 1721011	1:2000	1:2000

**Extended Data Table 4. List of antibodies used in the study.**

**Extended Data references:**

1. Muhleip, A., McComas, S.E. & Amunts, A. Structure of a mitochondrial ATP synthase with bound native cardiolipin. *Elife* **8**, e51179 (2019).
2. Larkin, M.A. et al. (2007). Clustal W and Clustal X version 2.0. *Bioinformatics*, **23**, 2947-2948 (2007).
3. Burki, F., Roger, A.J., Brown, M.W. & Simpson, A.G.B. The New Tree of Eukaryotes. *Trends Ecol Evol* **35**, 43-55 (2020).
4. Protein Sequence Similarity Search. *Curr Protoc Bioinformatics* **60**, 3151-31523 (2017).
5. Huang, Y., Niu, B., Gao, Y., Fu, L. & Li, W. CD-HIT Suite: a web server for clustering and comparing biological sequences. *Bioinformatics* **26**, 680-2 (2010).
6. Sievers, F. et al. Fast, scalable generation of high-quality protein multiple sequence alignments using Clustal Omega. *Mol Syst Biol* **7**, 539 (2011).
7. Edgar, R.C. MUSCLE: multiple sequence alignment with high accuracy and high throughput. *Nucleic Acids Res* **32**, 1792-7 (2004).

## Supplementary Files

This is a list of supplementary files associated with this preprint. Click to download.

- [Video1.mp4](#)
- [Video2.mp4](#)
- [Video3.mp4](#)